

# Di-neutron correlation and soft dipole excitation in medium mass neutron-rich nuclei near drip-line

Masayuki Matsuo, Kazuhito Mizuyama, Yasuyoshi Serizawa

*Graduate School of Science and Technology, Niigata University, Niigata 950-2181, Japan*

(Dated: December 13, 2018)

The neutron pairing correlation and the soft dipole excitation in medium-mass nuclei near drip-line are investigated from a viewpoint of the di-neutron correlation. Numerical analyses by means of the coordinate-space HFB and the continuum QRPA methods are performed for even-even  $^{18-24}\text{O}$ ,  $^{50-58}\text{Ca}$  and  $^{80-86}\text{Ni}$ . A clear signature of the di-neutron correlation is found in the HFB ground state; two neutrons are correlated at short relative distances  $\lesssim 2$  fm with large probability  $\sim 50\%$ . The soft dipole excitation is influenced strongly by the neutron pairing correlation, and it accompanies a large transition density for pair motion of neutrons. This behavior originates from a coherent superposition of two-quasiparticle configurations  $[l \times (l+1)]_{L=1}$  consisting of continuum states with high orbital angular momenta  $l$  reaching an order of  $l \sim 10$ . It raises a picture that the soft dipole excitation under the influence of neutron pairing is characterized by motion of di-neutron in the nuclear exterior against the remaining  $A - 2$  subsystem. Sensitivity to the density dependence of effective pair force is discussed.

PACS numbers: 21.10.Ky, 21.10.Re, 21.60.Jz, 24.30.Cz, 25.60.Gc

## I. INTRODUCTION

Excitations of neutron-rich nuclei near drip-line are subjects which are currently investigated extensively. It is expected that exotic properties such as halo, skin or presence of weakly bound nucleons in neutron-rich nuclei cause new features in excitations. An example is the soft dipole excitation in light halo nuclei[1, 2, 3, 4, 5, 6, 7, 8], typically in  $^{11}\text{Li}$  and  $^{11}\text{Be}$ , where significant E1 strength is observed above the very low neutron threshold energy. This is in contrast to the situation in stable nuclei, where most of the E1 strength concentrates in the high energy region of giant resonances. Recently the soft dipole excitation is observed also in heavier systems up to neutron-rich oxygen isotopes  $^{18-22}\text{O}$  [9, 10]. These oxygen isotopes do not exhibit noticeable halo structure[11], but on the other hand they contain many valence neutrons. This suggests that the soft dipole excitation is not always inherent to one- or two-neutron halo, but instead it may be a many-body phenomenon more generally seen in many neutron-rich nuclei near drip-line reaching medium and possibly heavier mass regions.

The degree of collectivity or the nature of correlations responsible for this excitation is one of the central issues which need to be clarified. Indeed different mechanisms have been proposed so far. One of the simplest mechanisms producing the soft dipole excitation is the one which is associated with uncorrelated excitation of a weakly bound neutron to continuum states. In this case, significant E1 strength emerges just above the threshold energy of neutron escaping without resorting to correlations nor collectivity, as it is sometimes called the threshold effect[12, 13]. This arises from a large spatial overlap between the extended wave function of a weakly bound single-particle orbit, which is occupied by a neutron in the ground state, and that of low energy continuum orbits, to which the neutron is excited. Major aspects of the soft dipole excitation observed in one-neutron halo systems, e.g.  $^{11}\text{Be}$ , fit rather well with this uncorrelated excitation picture[4, 5]. However, when more than one neutrons participate in the excitation, correlation between neutrons plays a role, and different mechanisms of the soft dipole excitation can be expected. In the case of the two-neutron halo nucleus  $^{11}\text{Li}$ , the pairing correlation among halo neutrons plays a decisive role for the binding and formation of the halo [14, 15, 16, 17, 18]. It is suggested that the two halo neutrons in the ground state display an attractive correlation in such a way that they are spatially localized with respect to their relative distance, in a range smaller than the size of the nuclear matter radius[14, 16, 17]. The pairing correlation of this type or the di-neutron correlation in short is predicted to cause a strong enhancement on the soft dipole excitation in the two-neutron halo nucleus [14, 19, 20], or even to form a collective vibrational motion of the correlated halo neutrons against the rest of the system[15, 21]. Experimentally signatures of possible di-neutron correlation in the soft dipole excitation are obtained in  $^{11}\text{Li}$ [2], but strong neutron-neutron correlations are not probed in other experiments[1, 3].

The soft dipole excitation in medium mass nuclei has also been investigated theoretically, but with different viewpoints and results. The random phase approximation (RPA) calculations based on the Hartree-Fock models or the relativistic mean-field model predict that the soft dipole excitations has a character of uncorrelated neutron excitation carrying very little collectivity in the neutron-rich oxygen isotopes [22, 23, 24]. Note however that these RPA models do not take into account the pair correlations among neutrons. The shell model calculation[25] reproduces rather well with the experimental soft dipole strength in oxygen isotopes, but continuum effects are not included. Recently quasiparticle RPA (QRPA) calculations that include explicitly the neutron pairing corrections have been

performed[26, 27, 28, 29]. Most recent ones predict that the neutron pair correlation has a sizable effect on E1 strength of the soft dipole excitation in the medium mass region[28, 29]. This suggests that the neutron pair correlation is an important key to clarify the character of the soft dipole excitation in medium mass and heavier systems.

In the present paper, we analyze in detail pair correlation effects in the medium mass region with  $Z = 8 - 28$ , taking proton (semi-)magic oxygen, calcium and nickel isotopes as representative examples. Motivated by the debate on the light two-neutron halo nuclei, we pay special attention to possibilities of the di-neutron correlation in these medium mass nuclei. We will conclude that some features of the di-neutron correlation are indeed present rather generally in the ground state of the medium mass nuclei. Furthermore the di-neutron correlation brings about a characteristic and strong influence also on the soft dipole excitation.

Our analysis is based on the Hartree-Fock-Bogoliubov (HFB) method in the coordinate-space representation for description of the ground state, and the continuum quasiparticle random phase approximation (the continuum QRPA) for the excitations. The coordinate-space HFB theory[30, 31, 32] is beneficial for description of nuclei with pair correlations near drip-line in medium and heavier mass regions since it extends the general HFB theory[33] in such a way that contributions of weakly-bound and continuum orbits to the pair correlation is precisely treated on the same footing with all other nucleons through an explicit account of the coordinate-dependence of the pair potential and the quasiparticle wave functions. It is possible then to describe the excitations by generalizing the coordinate-space HFB to a time-dependent problem, i.e. by considering a linear response of the system against the external perturbation. We have formulated recently a new QRPA method[34] along this line to describe excitations embedded in the continuum region above the threshold energies of nucleon escaping, which is an essential feature of nuclei near drip-line. This continuum QRPA has several distinctive features, compared to the continuum RPA[23, 35, 36] which neglects the pair correlation, and to the conventional QRPA neglecting continuum effects. One of the most distinguished aspects is that it enables us to include correlations among continuum two-quasiparticle configurations corresponding to two-neutron escaping as well as to one-neutron escaping. As the model formulation is fully microscopic in treating all the nucleon degrees of freedom democratically, the di-neutron correlation, if present, emerges only as a consequence of the microscopic description. In order to probe the di-neutron behaviors in the ground state and in the soft dipole excitation we look into the two-body correlation density and the pair transition densities, which provide information on pair motion of neutrons.

Numerical calculations are performed for even-even neutron-rich oxygen, calcium and nickel isotopes  $^{18-24}\text{O}$ ,  $^{50-58}\text{Ca}$  and  $^{80-86}\text{Ni}$  near drip-line and for some more stable isotopes for comparison. In Section II, we analyze the di-neutron correlation in the HFB ground state. In Section III, analysis of the soft dipole excitations using the continuum QRPA method is presented. Conclusions are drawn in Section IV. We do not discuss in the present paper the low-lying dipole strength in stable nuclei with neutron excess, called pygmy dipole resonance [37, 38, 39, 40, 41] since the situations are different from those in near-drip-line nuclei on which we put focus in the present paper. Preliminary report of the present work is seen in Ref.[42].

## II. DI-NEUTRON CORRELATION IN THE GROUND STATE

### A. Coordinate-space HFB with density dependent interaction

Wave functions of weakly bound neutrons in nuclei close to drip-line extend largely to the outside of nuclear surface due to the quantum mechanical penetration. Since associated neutron density is very low, the pair correlations in internal, surface, and external regions may be different. The coordinate-space Hartree-Fock-Bogoliubov theory[30, 31, 32] enables us to deal with this non-uniformity by utilizing an explicit coordinate representation for the Bogoliubov quasiparticles, which are the fundamental modes of the single-particle motion under the influence of pairing correlation. In this scheme the quasiparticles are able to have both particle and hole characters simultaneously, and accordingly they are expressed by the two-component wave functions

$$\phi_{iq}(\mathbf{r}\sigma) \equiv \begin{pmatrix} \varphi_{1,iq}(\mathbf{r}\sigma) \\ \varphi_{2,iq}(\mathbf{r}\sigma) \end{pmatrix}, \quad (1)$$

where  $\sigma = \pm\frac{1}{2} = \uparrow, \downarrow$ , and  $q = n, p$  represent spin and isospin. The quasiparticle states are determined by the HFB equation

$$\mathcal{H}_{0q}\phi_{iq}(\mathbf{r}\sigma) = E_{iq}\phi_{iq}(\mathbf{r}\sigma), \quad (2)$$

with

$$\mathcal{H}_{0q} = \begin{pmatrix} h_q - \lambda_q & \tilde{h}_q \\ \tilde{h}_q & -h_q + \lambda_q \end{pmatrix} \quad (3)$$

where  $E_{iq}$  is the quasiparticle energy. The HFB selfconsistent mean-field Hamiltonian  $\mathcal{H}_{0q}$  consists of not only the particle-hole part  $h_q - \lambda_q$  including the kinetic energy term, the Hartree-Fock mean-field and the Fermi energy  $\lambda_q$ , but also the particle-particle part  $\tilde{h}_q$  originating from the pair correlation. The mean-field Hamiltonian,  $h_q$  and  $\tilde{h}_q$ , are expressed in terms of the normal density matrix  $\rho_q(\mathbf{r}\sigma, \mathbf{r}'\sigma') = \langle \Phi_0 | \psi_q^\dagger(\mathbf{r}'\sigma') \psi_q(\mathbf{r}\sigma) | \Phi_0 \rangle$ , the pair density matrix  $\tilde{\rho}_q(\mathbf{r}\sigma, \mathbf{r}'\sigma') = \langle \Phi_0 | \psi_q(\mathbf{r}'\sigma') \psi_q(\mathbf{r}\sigma) | \Phi_0 \rangle = (-2\sigma) \langle \Phi_0 | \psi_q(\mathbf{r}' - \sigma') \psi_q(\mathbf{r}\sigma) | \Phi_0 \rangle$  and the effective nuclear force. We do not need the explicit form of the correlated HFB ground state  $|\Phi_0\rangle$  since ground state expectation values of various physical quantities can be evaluated with use of the Wick's theorem for the quasiparticle annihilation and creation operators  $\beta_{iq}$  and  $\beta_{iq}^\dagger$  satisfying the vacuum condition  $\beta_{iq} |\Phi_0\rangle = 0$ , and with use of their relation to the nucleon annihilation and creation operators given by

$$\begin{aligned}\psi_q(\mathbf{r}\sigma) &= \sum_i \varphi_{1,iq}(\mathbf{r}\sigma) \beta_{iq} - \varphi_{2,iq}^*(\mathbf{r}\bar{\sigma}) \beta_{iq}^\dagger, \\ \psi_q^\dagger(\mathbf{r}\sigma) &= \sum_i \varphi_{1,iq}^*(\mathbf{r}\sigma) \beta_{iq}^\dagger - \varphi_{2,iq}(\mathbf{r}\bar{\sigma}) \beta_{iq}.\end{aligned}\quad (4)$$

In the present work, we derive the particle-particle mean-field  $\tilde{h}_q$  by using the selfconsistent HFB scheme. As the effective nuclear force responsible for the particle-particle part  $\tilde{h}_q$ , called shortly the effective pairing force below, we adopt the density dependent delta interaction [14, 43, 44]

$$v_{pair}(\mathbf{r}, \mathbf{r}') = \frac{1}{2} V_0 (1 - P_\sigma) \left( 1 - \frac{\rho(\mathbf{r})}{\rho_0} \right) \delta(\mathbf{r} - \mathbf{r}'). \quad (5)$$

With this choice, the particle-particle part  $\tilde{h}_q$  becomes a local pair potential  $\Delta_q(\mathbf{r}) = \frac{V_0}{2} \left( 1 - \frac{\rho(\mathbf{r})}{\rho_0} \right) \tilde{\rho}_q(\mathbf{r})$  expressed with the diagonal pair density  $\tilde{\rho}_q(\mathbf{r}) = \sum_\sigma \tilde{\rho}_q(\mathbf{r}\sigma, \mathbf{r}\sigma)$ . The parameter  $\rho_0$  together with the total density  $\rho(\mathbf{r}) = \rho_n(\mathbf{r}) + \rho_p(\mathbf{r})$  in Eq.(5) controls the density dependence of the effective pairing force. There is no established knowledge on the density dependence of the pairing force, being under current investigations[45, 46, 47]. In the following analysis, we consider three cases: 1) the pairing with strong density dependence (or the surface pairing force in short), for which the parameter  $\rho_0$  is set to the central total density  $\rho_0 = 0.19 \text{ fm}^{-3}$ , 2) the density independent pairing force with the choice of  $1/\rho_0 = 0$  (the volume pairing force), and 3) the case of an intermediate density dependence with  $\rho_0 = 0.32 \text{ fm}^{-3}$  (the mixed pairing force). Since a recent analysis suggests that the mixed pairing reproduces better the odd-even mass difference in many isotopic chains[47], we adopt the mixed pairing as a reference choice. The surface and volume pairing forces are employed to examine sensitivity to the density dependence.

Concerning the particle-hole part  $h_q$  of the HFB Hamiltonian, we replace it by a spherical Woods-Saxon potential model in the present work for the simplicity of numerical calculation. The use of the Woods-Saxon model makes the continuum QRPA calculation feasible. To our knowledge, there is so far no fully selfconsistent continuum QRPA calculation that utilizes the full HFB Hamiltonian derived from an effective interaction. The parameters of the Woods-Saxon model follow Ref.[35], which gives a reasonable description of the giant dipole excitation in doubly shell-closed stable nuclei, such as  $^{16}\text{O}$  and  $^{40}\text{Ca}$ . Neutron single-particle orbits near the Fermi energy are shown in Fig.1 for representative isotopes.

Assuming the spherical symmetry, we solve the HFB equation (2) in the radial coordinate for each partial wave. Here we adopt the radial mesh size  $\Delta r = 0.2 \text{ fm}$ , and the box size  $r_{max} = 20 \text{ fm}$ , following Ref.[34]. A cut-off quasiparticle energy  $E_{max} = 50 \text{ MeV}$  and the angular momentum cut-off  $l_{max} = 12$  are used in summing up contributions of quasiparticle states when we evaluate the density matrices and associated quantities. Note that we include continuum quasiparticle states with  $E > |\lambda_q|$  which lie above the threshold energy  $|\lambda_q|$ . These continuum states, whose upper component  $\varphi_{1,iq}(\mathbf{r}\sigma)$  of the quasiparticle wave function extends to the outside of the nucleus without decaying, contribute to the correlated HFB ground state. To achieve the selfconsistency between the quasiparticle wave functions and the HFB mean-field Hamiltonian an iteration method[30] is used.

The force strength parameter  $V_0$  in Eq.(5) is fixed for each isotope chain so that the calculated neutron average gap  $\langle \Delta_n \rangle = \int \tilde{\rho}_n(\mathbf{r}) \Delta_n(\mathbf{r}) d\mathbf{r} / \int \tilde{\rho}_n(\mathbf{r}) d\mathbf{r}$  [30, 34, 51] gives an overall agreement with the odd-even mass difference of the three-point formula[48], as shown in Fig.2. A common value  $V_0 = -280 \text{ MeV fm}^3$  is adopted in the case of the mixed pairing. Note that we here improve the pairing force parameter, compared with our previous calculations[28, 34] where the conventional systematics  $\Delta_{syst} = 12/\sqrt{A} \text{ MeV}$  is fitted to determine  $V_0$ . The value of  $\Delta_{syst}$  in the oxygen isotopes is larger by about 40% than the experimental odd-even mass difference (Fig.2). In the following we shall use a larger value of  $V_0$  which corresponds to the value of  $\Delta_{syst}$  in order to investigate dependence on the pairing force strength.

## B. Two-body correlation density

In order to analyze spatial behavior of the neutron pair correlation and to search for possible di-neutron aspects, we evaluate the two-body correlation density

$$\rho_{corr,q}(\mathbf{r}\sigma, \mathbf{r}'\sigma') = \langle \Phi_0 | \sum_{i \neq j \in q} \delta(\mathbf{r} - \mathbf{r}_i) \delta(\mathbf{r}' - \mathbf{r}_j) \delta_{\sigma_i \sigma} \delta_{\sigma_j \sigma'} | \Phi_0 \rangle - \rho_q(\mathbf{r}\sigma) \rho_q(\mathbf{r}'\sigma') \quad (6)$$

for the calculated ground state. This quantity displays correlation between two neutrons at positions  $\mathbf{r}$  and  $\mathbf{r}'$  with spins  $\sigma$  and  $\sigma'$ . The spin anti-parallel (spin-singlet) configuration  $\sigma\sigma' = \uparrow\downarrow$  is responsible for the neutron pairing. In the above definition we subtract the uncorrelated contribution  $\rho_q(\mathbf{r}\sigma)\rho_q(\mathbf{r}'\sigma')$  in order to separate the change originating from the correlation.

The two-body correlation density is also expressed as

$$\rho_{corr,q}(\mathbf{r}\sigma, \mathbf{r}'\sigma') = |\tilde{\rho}_q(\mathbf{r}\sigma, \mathbf{r}'\tilde{\sigma}')|^2 - |\rho_q(\mathbf{r}\sigma, \mathbf{r}'\sigma')|^2 \quad (7)$$

in terms of off-diagonal parts of the pair and the normal density matrices. For the spin anti-parallel configuration, the first term of Eq.(7) gives dominant contribution when the pair correlation is present. A different behavior is seen for the spin parallel configuration, where the two-body correlation density probes dominantly the Pauli repulsion effect, which is brought by the second term. In the following we concentrate on the spin anti-parallel neutron correlation. In displaying this quantity, we fix the position  $\mathbf{r}'$  of one spin-down ( $\sigma' = \downarrow$ ) neutron (called the reference neutron hereafter) and plot it as a function of the position  $\mathbf{r}$  of the other spin-up ( $\sigma = \uparrow$ ) neutrons. Actual plots are made for the two-body correlation density  $\rho_{corr,n}(\mathbf{r} \uparrow, \mathbf{r}' \downarrow) / \rho_n(\mathbf{r}' \downarrow)$  divided by the neutron density  $\rho_n(\mathbf{r}' \downarrow)$  at the position of the reference neutron. This represents the conditional probability of finding neutrons at position  $\mathbf{r}$  with spin  $\sigma = \uparrow$  provided that the reference neutron is fixed at  $\mathbf{r}'$  with spin  $\sigma' = \downarrow$ . This normalization removes the trivial radial dependence of the density that falls off exponentially as the reference neutron position moves to the exterior region. This facilitates comparison among different positions of the reference neutron.

Examples of the two-body correlation density are displayed in Fig.3 for nuclei near drip-line  $^{22}\text{O}$ ,  $^{58}\text{Ca}$  and  $^{84}\text{Ni}$ . The reference neutron is placed at a position  $\mathbf{r}' = (0, 0, z')$  along the z-axis, where  $z'$  is fixed the surface radius  $z' = R_{surf}$ . We evaluate  $R_{surf}$  by a position of the half central neutron density. To examine dependence on the reference neutron position, it is further displaced at an internal ( $z' = R_{surf} - 2$  fm) and an external ( $z' = R_{surf} + 2$  fm) positions shifted by  $\pm 2$  fm from the surface. The external position  $z' = R_{surf} + 2$  fm represents the neutron skin region, as the neutron density at this position is about  $\sim 1/30$  of the central density (see Fig.6) in these isotopes. (Note that a criterion  $\rho_n(\mathbf{r})/\rho_n(0) = 1/100$  is sometimes adopted in the literature [49, 50] to define the neutron skin thickness and to distinguish from a typical neutron halo, which emerges with a lower density  $\rho_n(\mathbf{r})/\rho_n(0) < 1/100$ .)

It is seen that the correlation density  $\rho_{corr,n}(\mathbf{r} \uparrow, \mathbf{r}' \downarrow)$  exhibits a large and sharp peak in all the cases shown in Fig.3. The peak position almost coincides with the reference neutron position. The width  $\xi_d$ , evaluated by the full width at half maximum, of the peak of the correlation density is only about 2 fm when the reference neutron is placed at the internal or the surface positions. This obviously means a strong concentration of the correlation density around the reference neutron as the width  $\xi_d$  is smaller than the nuclear radius or the distance between the reference neutron and the nuclear center. In the region other than the first largest peak, the correlation density displays oscillatory behaviors, but its absolute value is much smaller than the first largest peak. The observed concentration of the two-body correlation density in the small region around the reference neutron indicates that two neutrons with spin anti-parallel (spin singlet) configuration has a large probability to come close at short relative distances  $|\mathbf{r} - \mathbf{r}'| \lesssim 2$  fm. It may be possible to regard this feature of the neutron pairing as that of the di-neutron correlation.

It is possible to quantify the extent of the di-neutron correlation by evaluating the first largest peak in the two-body correlation density. Here we note that the first term in Eq.(7) gives the dominant contribution to the correlation density. This term expressed in terms of the pair density matrix has a direct relation to the pair correlation. It is customary to regard the pair density matrix  $\tilde{\rho}_n(\mathbf{r}\sigma, \mathbf{r}'\tilde{\sigma}')^* = \langle \Phi_0 | \psi_n^\dagger(\mathbf{r}\sigma) \psi_n^\dagger(\mathbf{r}'\tilde{\sigma}') | \Phi_0 \rangle$  as the wave function of a neutron pair in the correlated HFB ground state. In this sense the first term  $|\tilde{\rho}_n(\mathbf{r}\sigma, \mathbf{r}'\tilde{\sigma}')|^2 \equiv p_n(\mathbf{r}\sigma, \mathbf{r}'\tilde{\sigma}')$  with the opposite spins represents the probability distribution of a spin-singlet neutron pair. Using this quantity and normalizing, we can define a relative probability

$$p(r_d) = \frac{\int_{|\mathbf{r}-\mathbf{r}'| < r_d} p_n(\mathbf{r} \uparrow, \mathbf{r}' \downarrow) d\mathbf{r}}{\int p_n(\mathbf{r} \uparrow, \mathbf{r}' \downarrow) d\mathbf{r}} \quad (8)$$

for the spin-up neutron to exist within a distance  $r_d$  from the spin-down reference neutron. The quantity  $p(r_d)$  with a suitable value of  $r_d$  measures the probability for the correlated neutron pair to form the di-neutron peak. We call it the di-neutron probability in the following. Calculated examples of the di-neutron probability are listed in Table

I. We adopt  $r_d = 2$  fm for the internal and the surface cases, while for the external case  $r_d = 3$  fm is chosen to cover the large peak near the reference neutron (cf. Figs.3, 7 and 8). The di-neutron probability amounts to 30-60%. As a reference, we compare with an estimate which would be obtained if the neutron pair probability  $p_n(\mathbf{r} \uparrow, \mathbf{r}' \downarrow)$  distributed uniformly in the whole nuclear volume. This uniform limit, which we evaluate by replacing  $p_n(\mathbf{r} \uparrow, \mathbf{r}' \downarrow)$  with the neutron density  $\rho_n(\mathbf{r})$ , gives  $p(r_d) = 0.20, 0.10, 0.06$  for  $z' = R_{surf} - 2, +0, +2$  fm in  $^{22}\text{O}$ ,  $0.08, 0.04, 0.03$  in  $^{58}\text{Ca}$ , and  $0.05, 0.03, 0.02$  in  $^{84}\text{Ni}$ . In contrast to the uniform limit, the microscopically calculated values of  $p(r_d)$  shown in Table I exhibit an significant enhancement especially at the surface and the external positions.

The di-neutron correlation emerges systematically at different positions inside and outside the nucleus, as seen in Fig.3. Inspecting in more detail, we find that, besides the width mentioned above, features of the di-neutron correlation vary with the reference neutron position. When the reference neutron is moved from the internal position ( $z' = R_{surf} - 2$  fm) to the surface ( $z' = R_{surf}$ ), the di-neutron correlation apparently enhances. This is also seen in the di-neutron probability (see the cases of  $^{22}\text{O}$ ,  $^{58}\text{Ca}$  and  $^{84}\text{Ni}$  in Table I), which shows an increase from  $p(r_d) \approx 30 - 40\%$  at the internal position to  $\approx 50\%$  at the surface position. Moving further toward the outside, as represented by the external position in the skin region  $z' = R_{surf} + 2$  fm, the concentration of correlation density around the largest peak is constantly quite large, keeping the di-neutron probability  $p(r_d) \approx 50 - 60\%$ . It is seen in this case that the peak position of the correlation density deviates slightly from the reference neutron position. The deviation is however within the di-neutron width  $\xi_d$ , keeping a large spatial overlap of the other neutron with the reference one. As the reference neutron moves far outside the nucleus, the deviation from the reference neutron increases further whereas the spatial correlation survives rather robustly even around  $z' \sim R_{surf} + 3$  to  $+4$  fm in  $^{58}\text{Ca}$  and  $^{84}\text{Ni}$ . (An example of the correlation density with  $z' = R_{surf} + 3$  fm is shown in Fig.4.) This behavior also manifests itself in the pair probability  $p(r_d)$ : In  $^{58}\text{Ca}$  for example, this quantity with the reference neutron positions  $z' = R_{surf} + 2, +3, +4$  and  $+5$  fm reads  $p(r_d) = 0.59, 0.57, 0.52$  and  $0.53$  with  $r_d = 3, 4, 5$  and  $6$  fm chosen respectively to encompass the first largest peak whereas  $p(r_d)$  with fixed  $r_d (= 3$  fm) decreases as  $p(r_d) = 0.59, 0.38, 0.18, 0.07$  at the same reference positions. We find a similar behavior in  $^{84}\text{Ni}$  while in  $^{22}\text{O}$  the strong concentration of two-body correlation density is seen for  $z' \lesssim R_{surf} + 3$  fm. The above observations indicate that the di-neutron correlation is most strong in the surface and the skin regions while the spatial correlation associated with the di-neutron behavior remains and decreases only gradually even outside the skin.

If we compare the oxygen, the calcium and the nickel isotopes in Fig.3, we observe that the concentration of two-body correlation density around the position of reference neutron is more evident in  $^{58}\text{Ca}$  and  $^{84}\text{Ni}$  than in  $^{22}\text{O}$ . For example, the di-neutron probability in  $^{58}\text{Ca}$  and  $^{84}\text{Ni}$  is as large as the one in  $^{22}\text{O}$  (Table I). This means that the enhancement relative to the uniform limit is much larger in  $^{58}\text{Ca}$  and especially in  $^{84}\text{Ni}$  than in  $^{22}\text{O}$ . It is also seen that the oscillatory behavior apart from the largest peak is weaker in  $^{58}\text{Ca}$  and  $^{84}\text{Ni}$  than in  $^{22}\text{O}$ , especially when the reference neutron is placed at the external position. The small oscillation is a remnant of nodal structure in the wave functions of neutron single-quasiparticle states near the Fermi energy, e.g.,  $2s_{1/2}$  and  $1d_{5/2,3/2}$  neutron states in the case of  $^{22}\text{O}$  although the magnitude of oscillation is suppressed by coherent contributions of other neutron quasiparticle states (see the next subsection for details). The smearing of the single-particle structures is more effective in heavier systems as more single-particle levels participate in the pairing correlation. It should be noted also that among the three isotopes the neutron separation energy (related to the Fermi energy) is smaller in  $^{58}\text{Ca}$  and especially in  $^{84}\text{Ni}$  than in  $^{22}\text{O}$  (see Fig.1). This difference in the neutron binding also influences the neutron pairing correlation in the external region as discussed just below.

We have also analyzed the neutron two-body correlation density along the isotopic chains of Ca and Ni to check the di-neutron property in more stable nuclei and to examine how the di-neutron correlation varies with approaching the neutron drip-line. We select  $^{44}\text{Ca}$  and  $^{66}\text{Ni}$  as examples representing stable nuclei and neutron-rich unstable nuclei (situated between the drip-line and the stable region), respectively. Here  $^{66}\text{Ni}$  is chosen to compare with the near-drip-line nucleus  $^{58}\text{Ca}$  having the same neutron number  $N = 38$ , and also with the near-drip-line isotope  $^{84}\text{Ni}$ . It is found that the gross behavior of the two-body correlation density in  $^{44}\text{Ca}$  and  $^{66}\text{Ni}$  is similar to those in  $^{58}\text{Ca}$  and  $^{84}\text{Ni}$  in the surface and the internal regions. As a representative example, we show in Fig.5 the two-body correlation density in  $^{44}\text{Ca}$  and  $^{66}\text{Ni}$  for the reference neutron fixed at the surface ( $z' = R_{surf}$ ). In Table I we do not see obvious difference between the near-drip-line nuclei and the more stable ones in the di-neutron probabilities  $p(r_d)$  at the internal position  $z' = R_{surf} - 2$  fm and at the surface  $z' = R_{surf}$ .

A clear difference emerges, however, as the reference neutron is placed far outside the nuclear surface. This is illustrated by Fig.4, where we compare the correlation densities in  $^{66}\text{Ni}$ ,  $^{84}\text{Ni}$  and  $^{58}\text{Ca}$  with a reference neutron fixed at a position ( $z' = R_{surf} + 3$  fm) in the far outside region. It is seen that the value of the correlation density evaluated at the reference neutron position is lower in  $^{66}\text{Ni}$  by a factor of two or more than in near-drip-line nuclei  $^{58}\text{Ca}$  and  $^{84}\text{Ni}$ . It is also seen that the large correlation density at the position of the reference neutron is most significant in  $^{84}\text{Ni}$ . This indicates that the di-neutron correlation in the external region is stronger in near-drip-line nuclei having shallower neutron Fermi energy than that in more stable nuclei with deeper Fermi energy (see Fig.1 for the single-particle energies and the Fermi energy in these nuclei). We can see directly this property also in the profiles

of the pair density  $\tilde{\rho}_n(r)$  of neutrons, shown in Fig.6. The pair density  $\tilde{\rho}_n(r)$  has comparable or larger magnitude  $\tilde{\rho}_n(r) \gtrsim \rho_n(r)$  with the normal density  $\rho_n(r)$  in the skin region  $r \sim R_{surf} + 2$  fm and far outside. As discussed in Ref.[31], the exponential tail constant of the neutron pair density  $\tilde{\rho}_n(r)$  in the asymptotic external region is related to the Fermi energy. The asymptotic tail develops as the drip line is approached, and is longer than that of the normal density  $\rho_n(r)$ . Consequently the di-neutron correlation in the external low density region becomes relatively stronger in nuclei near neutron drip-line.

### C. Di-neutron correlation and single-particle configurations

In obtaining the significant di-neutron correlation, it is essential to adopt a large model space of neutron quasiparticle states including continuum orbits up to large quasiparticle energy ( $E_{max} = 50$  MeV in the present calculation) and large orbital angular momentum ( $l_{max} = 12$ ). On the contrary, significant di-neutron correlation would not be obtained if we used a small single-particle model space.

In the case of the oxygen isotopes, for example, one may consider that neutron single-particle orbits  $2s_{1/2}$  and  $1d_{5/2,3/2}$  lying around the neutron Fermi energy are those most responsible for the neutron pairing. (Note that the Woods-Saxon  $1d_{3/2}$  orbit is not a bound orbit but a resonance close to the zero energy. See Fig.1.) However, if one truncates to a single- $j$  orbit or to orbits in one major shell, the di-neutron correlation never shows up. This is because the two-body correlation density would exhibit a mirror symmetry with respect to the  $x$ - $y$  plane if only orbits with the same parity are taken into account. Apparently one needs more single-particle orbits with additional orbital angular momenta having different parities.

In Fig.7, we show partial contributions of neutron quasiparticle orbits truncated with respect to the orbital angular momentum  $l$  of the orbits. Namely the two-body correlation density is evaluated by including the neutron quasiparticle states only up to a cut-off orbital angular momentum  $l_{cut}$ . Inclusion of low angular momenta  $l = 0, 1, 2$  covering at least all the neutron bound Woods-Saxon single-particle orbits in  $^{22}\text{O}$  is insufficient to bring about the di-neutron correlation at the surface and the external positions; see the line corresponding to  $l_{cut} = 2$ . If we add  $l = 3$   $f_{7/2,5/2}$  orbits ( $l_{cut} = 3$ ), the di-neutron correlation becomes more visible, but an approximate convergence is achieved only by including further  $l = 4 - 5$  orbits. It should be noted here that the neutron quasiparticle orbits with high angular momentum ( $l > 2$ ) are continuum states with  $E > |\lambda_n|$ . It is the pair correlation that makes these high- $l$  continuum orbits to contribute to the ground state pair correlation. Fig.7 indicates that the continuum high- $l$  orbits are important also for Ca and Ni isotopes, for which a larger value of angular momenta up to  $l \sim 6 - 8$  at  $z' = R_{surf}$  and  $l \sim 7 - 9$  at  $z' = R_{surf} + 2$  fm are necessary.

The large contribution of the neutron high- $l$  quasiparticle orbits is related to the fact that the di-neutron correlation has a characteristic small width  $\xi_d \sim 2$  fm, which indicates an attraction within a short relative distance between two neutrons. It is illustrative to consider a pair of neutrons which are correlated in the *relative s-wave* at zero relative distance, and whose center of gravity is located off the nuclear center. A corresponding two particle wave function is written as  $\sim \delta(\mathbf{r} - \mathbf{r}') \propto \sum_{lm} Y_{lm}^*(\mathbf{r}) Y_{lm}(\mathbf{r}')$  where  $l$  is the orbital angular momentum about the nuclear center. This expression indicates that a coherent superposition of orbits with all orbital angular momenta  $l$  are necessary for such a correlation. On a similar basis, we can argue that a superposition of angular momenta up to  $l_M$  is needed to describe the di-neutron correlation which is dominantly in the relative *s-wave* and has a width approximately given by  $\xi_d \sim 2r/l_M$  ( $r$  being the radial position of the center of gravity of the pair). This estimate based on the observed di-neutron width  $\xi_d \sim 2$  fm gives a qualitative (though not precise) account of the maximum angular momentum seen in Fig.7.

We have also examined contribution of the orbits by truncating the neutron quasiparticle states up to a cut-off quasiparticle energy  $E_{cut}$ . Results are shown in Fig.8. The di-neutron correlation never appears only with the small model space including only up to  $E_{cut} = 5$  MeV, which usually covers most of the quasiparticle states in one major shell. The results with cut-off of  $E_{cut} = 10, 20$  MeV display only weak di-neutron correlation, and one needs neutron quasiparticle states at least up to  $E \sim 30$  MeV to obtain a qualitative account of the di-neutron correlation. As the neutron Fermi energy is small ( $-\lambda_n = 3.54, 2.13,$  and  $0.72$  MeV in the case of  $^{22}\text{O}$ ,  $^{58}\text{Ca}$ , and  $^{84}\text{Ni}$ , respectively), the quasiparticle states that contribute to the di-neutron correlation are mostly those embedded in the continuum energy region  $E > |\lambda_n|$ . Most of the neutron continuum states are non-resonant states except for a few corresponding to the hole neutron orbits (e.g.  $1p_{1/2,3/2}$  and  $1s_{1/2}$ ) which have specific quasiparticle energies. The slow convergence with respect to the quasiparticle energy indicates that the non-resonant continuum states give non-negligible and accumulating contributions to the di-neutron correlation. It is noted that contribution of quasiparticle states with relatively small quasiparticle energy is important in the case of the external position. This may be related to the fact the pair correlation becomes weaker in the external region.

### D. Dependence on pair interaction

We have examined also dependence of the di-neutron correlation on the pairing force strength  $V_0$ . Here  $V_0$  is varied from the reference value  $V_0 = -280 \text{ MeVfm}^3$  (which produces  $\langle\Delta_n\rangle = 1.5 \text{ MeV}$  corresponding to the experimental gap in  $^{22}\text{O}$ ) to an increased value  $V_0 = -350 \text{ MeVfm}^3$  ( $\langle\Delta_n\rangle = 2.8 \text{ MeV}$  corresponding to the conventional systematics  $\Delta_{\text{sys}} = 12/\sqrt{A} \text{ MeV}$ ). Results are shown in Fig.9. It is noted that increase of the pairing force strength  $V_0$  enhances the di-neutron correlation, i.e., increases the intensity of only the first largest peak, rather than causing overall enhancement of the two-body correlation density. This indicates that the di-neutron behavior is indeed a correlation effect caused by the attractive interaction among neutrons.

It is expected that the density dependence of the pairing interaction influences the di-neutron correlation since the pairing force of the surface and the mixed types give stronger neutron-neutron attraction in the surface and the external regions than in the interior. The volume pairing force (the density independent force) does not have this feature. To examine the influence of the density dependence, we perform calculations with use of the surface and the volume pairing forces. The pairing force strength  $V_0$  is chosen to reproduce the same average pairing gap  $\langle\Delta_n\rangle$  calculated with the mixed pairing force. The calculated two-body correlation density is shown in Fig.10. It indicates that the density dependence indeed affects the di-neutron correlation. Namely, in the case of surface pairing, the calculated two-body correlation density is significantly large in the surface (e.g.  $z' = R_{\text{surf}}$ ) and the exterior regions ( $z' = R_{\text{surf}} + 2 \text{ fm}$ ) but it is weak in the internal region ( $z' = R_{\text{surf}} - 2 \text{ fm}$ ). The volume pairing force does not exhibit such a position dependence. In the case of the mixed pairing force, the two-body correlation displays an intermediate feature as seen from comparison of Figs.7 and 10.

We emphasize also that the di-neutron correlation cannot be properly described if one adopts the schematic seniority pairing force used together with the conventional BCS approximation, where a constant pairing gap  $\Delta_0$  is assumed instead of the selfconsistent pair potential  $\Delta(\mathbf{r})$ . This is illustrated in Fig.11, where we present a BCS calculation obtained with use of the standard analytic expression of  $u, v$ -factors, the Woods-Saxon single-particle energies, and the gap constant  $\Delta_0$ . We include all bound and discretized continuum Woods-Saxon neutron orbits (obtained with the box radius  $r_{\text{max}} = 20 \text{ fm}$ ), and use the same cut-off parameters  $E_{\text{max}} = 50 \text{ MeV}$  and  $l_{\text{max}} = 12$  as in the HFB calculation. The value of  $\Delta_0$  is set to that of the average neutron gap  $\langle\Delta_n\rangle$  obtained in the HFB calculation. It is seen that the BCS calculation causes a significant overestimate of the correlation density when the reference neutron is placed at external positions. In the case of surface and internal positions, the disagreement with the HFB is less serious, but profiles of the two-body correlation density are not well reproduced, as shown in Fig.11. The unwanted overestimate in the external region arises from contributions of the discretized Woods-Saxon orbits in the positive-energy continuum region, for which the BCS approximation is known to cause unphysical correlation[31]. If we neglect the discretized continuum Woods-Saxon orbits to avoid this difficulty, however, the BCS approximation produces a result (dotted line in Fig.11) which is far off the HFB result, and the di-neutron correlation never shows up.

### E. Di-neutron size and coherence length

The small width  $\xi_d \sim 2 \text{ fm}$  of the di-neutron correlation, or the di-neutron size in short, provides a characteristic length scale of the neutron pairing correlation. We note that this di-neutron size should be distinguished from the coherence length (the Pippard's coherence length), which plays a central role in the standard BCS theory of the metal superconductivity. The Pippard's coherence length for a superconducting uniform matter is given analytically as  $\xi_P = \hbar v_F / \pi \Delta$  with  $v_F$  and  $\Delta$  being the Fermi velocity and the pairing gap[52]. A direct application of  $\xi_P$  to the nuclear case with typical values of  $v_F$  and  $\Delta$  gives the coherence length of an order of 10fm which is larger than the nuclear radius. If this estimate is adopted, the wave function of neutron pairs is meant to extend in the whole region of nuclear volume[53]. The present numerical investigation, however, reveals that the probability distribution of the neutron pair wave function is far from uniform, and a large probability  $\sim 50\%$  is concentrated in a small region with short relative distances  $|\mathbf{r} - \mathbf{r}'| \lesssim 2 \text{ fm}$  while the rest probability spreads in the whole nuclear volume. Our finding suggests that we may need at least two length scales (one is the di-neutron size and the other is the coherence length) to characterize the nuclear pairing correlation.

We note also that the two-neutron correlation is calculated by Barranco et al.[54] in a microscopic HFB description of the neutron pairing in the non-uniform low density neutron matter in a Wigner-Seitz cell with a immersed lattice 'nucleus', approximating the situation of an inner crust of neutron stars. The authors point out that the root mean square relative distance weighted with the two-neutron probability density coincides approximately with the Pippard's coherence length  $\xi_P$ . The calculated two-neutron probability itself (Fig.3 in Ref.[54]), on the other hand, shows a distribution that forms a sharp and large peak at short relative distances  $|\mathbf{r} - \mathbf{r}'| \lesssim 2 \text{ fm}$ , indicating a behavior similar to the di-neutron correlation discussed in the present investigation. This might suggest that the presence of the di-neutron correlation with a small length scale  $\sim 2 \text{ fm}$  is a quite general feature of the nuclear pairing correlation. The

HFB calculation in Ref.[54] adopts the finite range Gogny force as the effective pairing force. Combining the results of Ref.[54] and ours, it can be suggested that the qualitative feature of the di-neutron correlation persists irrespective of detailed forms of the effective pairing force. The quantitative aspects however will depend on the effective interaction as we already discussed in the previous subsection.

### III. DI-NEUTRON CORRELATION IN THE SOFT DIPOLE EXCITATION

#### A. Continuum QRPA description of the soft dipole excitation

We first recapitulate briefly the continuum QRPA method[34] which we adopt to describe the dipole excitation of nuclei near drip-line. It provides a fully microscopic description of a linear response of the nucleus excited by an external perturbing field with taking into account all nucleon degrees of freedom. It is formulated as the small amplitude limit of a time-dependent extension (TDHFB) of the coordinate-space HFB theory, which we utilize for the description of the ground state. Consequently the description is constructed in a selfconsistent manner. The linear responses in the normal and the pair densities are the basic quantities of the description. They are governed by the RPA density response equation called also the Bethe-Salpeter equation[33]:

$$\begin{pmatrix} \delta\rho_{qL}(r, \omega) \\ \delta\tilde{\rho}_{+,qL}(r, \omega) \\ \delta\tilde{\rho}_{-,qL}(r, \omega) \end{pmatrix} = \int_0 dr' \begin{pmatrix} R_{0,qL}^{\alpha\beta}(r, r', \omega) \end{pmatrix} \begin{pmatrix} \sum_{q'} \kappa_{ph}^{qq'}(r') \delta\rho_{q'L}(r', \omega)/r'^2 + v_{qL}^{ext}(r') \\ \kappa_{pair}(r') \delta\tilde{\rho}_{+,qL}(r', \omega)/r'^2 \\ -\kappa_{pair}(r') \delta\tilde{\rho}_{-,qL}(r', \omega)/r'^2 \end{pmatrix}. \quad (9)$$

Here the excitation with multipolarity  $L$  and frequency  $\omega$ , and use of contact forces are assumed. The functions  $\kappa_{ph}(r)$  and  $\kappa_{pair}(r)$  represent the residual interaction associated with the density variations. An important feature of the present response equation is that we here include the particle-particle channel, i.e., the second and the third rows in Eq.(9) containing  $\delta\tilde{\rho}_{+,qL}(r', \omega)$  and  $\delta\tilde{\rho}_{-,qL}(r', \omega)$ , which correspond to the variations in the pair densities  $\delta\tilde{\rho}_{\pm,q}(\mathbf{r}t) = \delta \langle \Phi(t) | \frac{1}{2} \sum_{\sigma} (\psi_q^{\dagger}(\mathbf{r}\sigma) \psi_q^{\dagger}(\mathbf{r}\tilde{\sigma}) \pm \psi_q(\mathbf{r}\tilde{\sigma}) \psi_q(\mathbf{r}\sigma)) | \Phi(t) \rangle$  as well as the one in the normal density  $\delta\rho_q(\mathbf{r}t) = \delta \langle \Phi(t) | \sum_{\sigma} \psi^{\dagger}(\mathbf{r}\sigma) \psi(\mathbf{r}) | \Phi(t) \rangle$  in the particle-hole channel, represented by the first row. To derive Eq.(9), a linear perturbation in the time-evolving TDHFB state vector  $|\Phi(t)\rangle$  is considered. The products  $\kappa_{pair}(r) \frac{1}{r^2} \delta\tilde{\rho}_{\pm,qL}(r, \omega)$  of the residual interaction  $\kappa_{pair}(r)$  and the pair density variations represent the dynamical change  $\delta\Delta(\mathbf{r}t)$  of the pair potential associated with the time-evolution. The two-point function  $R_{0,qL}^{\alpha\beta}(r, r', \omega)$  is the unperturbed response function for the three kinds of densities  $\rho(r)$  and  $\tilde{\rho}_{\pm}(r)$ , which are indexed by  $\alpha$  and  $\beta$ . Through the recursive relation for the density responses in Eq.(9), the RPA correlations with infinite orders of the residual interactions are taken into account. The RPA correlation acting in the particle-particle channel, which is associated with the residual pair interaction  $\kappa_{pair}$ , may be called the *dynamical pair correlation*[28, 29, 34]. As the external field, whose radial form factor is represented by  $v_{qL}^{ext}(r)$ , we consider the dipole operator

$$D_{\mu} = e \frac{Z}{A} \sum_{i \in n} (r Y_{1\mu})(\mathbf{r}_i) - e \frac{N}{A} \sum_{i \in p} (r Y_{1\mu})(\mathbf{r}_i), \quad (10)$$

in which the spurious center of mass motion is explicitly removed. As the effective nuclear force, we adopt the density dependent delta forces. We employ the same pairing force  $v_{pair}$  used in the HFB description of the ground state to derive the particle-particle residual interaction  $\kappa_{pair}$ . Thus the selfconsistency is achieved in treating correlations in the particle-particle channel. As the effective force responsible for the particle-hole correlation, we adopt a delta interaction of the Skyrme type

$$v_{ph}(\mathbf{r}, \mathbf{r}') = (t_0(1 + x_0 P_{\sigma}) + t_3(1 + x_3 P_{\sigma}) \rho(\mathbf{r})) \delta(\mathbf{r} - \mathbf{r}'), \quad (11)$$

which gives a reasonable description of the giant resonances in closed-shell stable nuclei[35]. With this choice the residual interaction reads

$$\kappa_{ph}^{q=q'}(r) = \frac{t_0}{2}(1 - x_0) + \frac{t_3}{12}((5 + x_3)\rho(r) - (2 + 4x_3)\rho_q(r)), \quad (12)$$

$$\kappa_{ph}^{q \neq q'}(r) = t_0(1 + \frac{x_0}{2}) + \frac{t_3}{12}(5 + x_3)\rho(r), \quad (13)$$

$$\kappa_{pair}(r) = \frac{V_0}{2} \left( 1 - \frac{\rho(r)}{\rho_0} \right). \quad (14)$$



In the present continuum QRPA method, a special attention is paid for treatment of the continuum states that play essential roles for excitations embedded in the energy region above the threshold of nucleon escaping. To this end we evaluate the unperturbed response functions  $R_{0,qL}^{\alpha\beta}$  by means of an integral representation that uses a contour integral in the complex quasiparticle energy plane[34]:

$$R_{0,qL}^{\alpha\beta}(r, r', \omega) = \frac{1}{4\pi i} \int_C dE \sum_{lj, l'j'} \frac{\langle l'j' || Y_L || lj \rangle^2}{2L+1} \{ \text{Tr} \mathcal{A}_\alpha \mathcal{G}_{0,ql'j'}(r, r', E + \hbar\omega + i\epsilon) \mathcal{B}_\beta \mathcal{G}_{0,qlj}(r', r, E) + \text{Tr} \mathcal{A}_\alpha \mathcal{G}_{0,qlj}(r, r', E) \mathcal{B}_\beta \mathcal{G}_{0,ql'j'}(r', r, E - \hbar\omega - i\epsilon) \}. \quad (15)$$

Here  $\mathcal{G}_{0,qlj}(E) = (E - \mathcal{H}_{0,qlj})^{-1}$  is the HFB Green function in the partial wave  $lj$ , which describes propagation of nucleons under influence of the pair potential  $\Delta(r)$  and the particle-hole mean-field. We use the exact form of HFB Green function  $\mathcal{G}_{0,qlj}(E)$ [55], which is given as a product of the regular and out-going solutions of the HFB equation (2) so that  $\mathcal{G}_{0,qlj}(E)$  satisfies the out-going boundary condition appropriate for continuum quasiparticle states. The combined use of the integral representation Eq.(15) and the exact HFB Green function is the key ingredient of the present continuum QRPA method. Note that the present scheme takes precise account of two quasiparticle configurations where two nucleons occupy simultaneously continuum orbits since the two quasiparticles are both described by the out-going HFB Green function in Eq.(15). Furthermore the particle-particle and the particle-hole correlations acting among such two-quasiparticle configurations are included through the density response equation (9). The energy-weighted sum rule (the TRK sum rule) is satisfied within about one percent thanks to the selfconsistent treatment of the pair correlations and the use of the exact HFB Green function. Detailed derivation and other aspects of the continuum QRPA method are discussed in Ref.[34].

Some physical quantities are calculated directly from the solution of the density response equation. The E1 strength function for the dipole excitation is given by  $S_{E1}(E = \hbar\omega) = dB(E1)/dE = -\frac{3}{\pi} \text{Im} \sum_q \int dr v_q^{ext}(r) \delta\rho_{qL=1}(r, \omega)$ . We can also characterize the excitation mode by means of the transition densities. The particle-hole transition density for an excited state  $|\Phi_i\rangle$ , at the excitation energy  $E_i$  (i.e. with the frequency  $\omega_i = E_i/\hbar$ ) is given by

$$\rho_{iq}^{ph}(\mathbf{r}) = \langle \Phi_i | \sum_{\sigma} \psi_q^{\dagger}(\mathbf{r}\sigma) \psi_q(\mathbf{r}\sigma) | \Phi_0 \rangle = Y_{LM}^*(\hat{\mathbf{r}}) \rho_{iqL}^{ph}(r), \quad (16)$$

$$\rho_{iqL}^{ph}(r) = -\frac{C}{\pi r^2} \text{Im} \delta\rho_{qL}(r, \omega_i) \quad (17)$$

with use of the density response  $\delta\rho_{qL}(r, \omega)$  in the particle-hole channel. We normalize the transition density by a constant  $C$  so that the transition amplitude for the E1 operator,  $M_{iq} = \int dr r^2 v_q^{ext}(r) \rho_{iqL}^{ph}(r)$ , gives the E1 strength  $B(E1, 0_{g.s.}^+ \rightarrow 1_i^-) = \int_{E_1}^{E_2} S_{E1}(E) dE = 3M_{iq}^2$  integrated over a certain energy interval around the excitation energy  $E = \hbar\omega_i$  of the state under consideration.

The present continuum QRPA also enables us to evaluate two kinds of transition amplitudes for pairs of nucleons:

$$P_{iq}^{PP}(\mathbf{r}) = \langle \Phi_i | \psi_q^{\dagger}(\mathbf{r}\uparrow) \psi_q^{\dagger}(\mathbf{r}\downarrow) | \Phi_0 \rangle = Y_{LM}^*(\hat{\mathbf{r}}) P_{iqL}^{PP}(r), \quad (18)$$

$$P_{iq}^{hh}(\mathbf{r}) = \langle \Phi_i | \psi_q(\mathbf{r}\downarrow) \psi_q(\mathbf{r}\uparrow) | \Phi_0 \rangle = Y_{LM}^*(\hat{\mathbf{r}}) P_{iqL}^{hh}(r). \quad (19)$$

These pair transition densities provide information of how nucleon pairs move in the excited state. The first pair transition density  $P_{iq}^{PP}(\mathbf{r})$  can be related to an amplitude to produce the excited state by adding (or transferring) at the position  $\mathbf{r}$  a spin-singlet nucleon pair with the relative  $s$ -wave to the ground state of the  $A-2$  system. We call it the particle-particle or the particle-pair transition density hereafter. The second pair transition density  $P_{iq}^{hh}(\mathbf{r})$ , which we call the hole-hole or the hole-pair transition density, on the other hand, is related to an amplitude of producing the excited state by removing a spin-singlet nucleon pair from the  $A+2$  ground state. These pair transition densities are calculated as

$$P_{iqL}^{PP}(r) = \frac{C}{2\pi r^2} \text{Im}(\delta\tilde{\rho}_{+,qL}(r, \omega_i) - \delta\tilde{\rho}_{-,qL}(r, \omega_i)), \quad (20)$$

$$P_{iqL}^{hh}(r) = \frac{C}{2\pi r^2} \text{Im}(\delta\tilde{\rho}_{+,qL}(r, \omega_i) + \delta\tilde{\rho}_{-,qL}(r, \omega_i)) \quad (21)$$

with use of the pair density responses  $\delta\tilde{\rho}_{\pm,qL}(r, \omega)$  obtained in the density response equation. Here the same normalization constant  $C$  is adopted as for the particle-hole transition density.

The force parameters of the particle-hole residual interaction is chosen as  $t_0 = -1100 \text{ MeVfm}^3$ ,  $t_3 = 16000 \text{ MeVfm}^3$ ,  $x_0 = 0.5$ , and  $x_3 = 1$  taken from Ref.[35]. To achieve an approximate selfconsistency in the particle-hole channel, a renormalization of the force strengths, i.e.,  $t_{0,3} \rightarrow f \times t_{0,3}$ [35] is adopted so that the lowest energy dipole mode

corresponding to the spurious center of mass motion has the zero excitation energy. The same radial mesh as in solving the HFB equation (2) is used to solve Eq.(9). The maximum orbital angular momentum in the two-quasiparticle sum of Eq.(9) is  $l_{max} = 12$  in O and Ca isotopes, which is the same as in the HFB calculation for the ground state. In Ni isotopes we use a larger value  $l_{max} = 17$  and a larger radius cut-off  $r_{max} = 25$  fm to achieve better convergence in the continuum QRPA calculations. In this case, the HFB calculation is performed with the enlarged  $l_{max}$  and  $r_{max}$  although we do not see any sizable influence in the ground state properties. The same mixed pairing force as that in the HFB calculation is adopted as the reference choice. We adopt a small imaginary constant with  $\epsilon = 0.2$  MeV, which corresponds to smoothing of the strength function convoluted with a Lorentzian with FWHM=0.4MeV. The calculated results shown below differ from those in the previous analysis[28], where calculations are done for  $^{22}\text{O}$  by using the surface-type pairing interaction ( $\rho_0 = 0.16 \text{ fm}^{-3}$ ) and a larger force strength  $V_0 = -520 \text{ MeVfm}^3$  adjusted to the conventional systematics of the pairing gap  $\Delta_{syst} = 12/\sqrt{A} \text{ MeV}$  ( $\sim 2.5 - 2.8 \text{ MeV}$  in the oxygen isotopes). Here the adopted value  $V_0 = -280 \text{ MeVfm}^3$  with  $\rho_0 = 0.32 \text{ fm}^{-3}$  is fixed so as to produce the odd-even mass difference ( $\sim 0.5 - 2.0 \text{ MeV}$ ) as discussed in Section II. Other numerical details are the same as in Ref.[28].

### B. E1 strength near neutron threshold energy

The E1 strength functions  $S_{E1}(E) = dB(E1)/dE$  calculated for even-even isotopes  $^{18-24}\text{O}$ ,  $^{50,54,58}\text{Ca}$ , and  $^{80-86}\text{Ni}$  near drip-line are presented in Fig.12. In all nuclides the strength function exhibits significant distribution of the E1 strength just above the threshold energy  $E_{th,1} = \min(E_{in}) + |\lambda_n|$  of one-neutron escaping and far below the giant dipole resonance energy ( $E_{GDR} \sim 20 \text{ MeV}$  in O and  $\sim 15 \text{ MeV}$  in Ni). This low-energy E1 strength increases significantly as the neutron drip-line is approached. In many isotopes the soft dipole excitation is situated also above the threshold energy  $E_{th,2} = 2|\lambda_n|$  of two-neutron escaping, which becomes low in nuclei near the drip-line and especially in the nickel isotopes. The strength distribution in the giant dipole resonance region shows also rather strong isotopic dependence in the case of the oxygen isotopes. The peak at the zero energy corresponds to the spurious center of mass motion, for which the energy weighted strength is negligible. In the following, we concentrate on the soft dipole excitations.

The strength function in the region of the soft dipole excitation shows a smooth profile as a function of the excitation energy. It is not possible to evaluate the resonance width as the strength does not form a sharp resonance peak. The smooth profile implies that neutron escaping has a large influence on the soft dipole excitations. This is explicitly seen by comparing with a calculation neglecting neutron escaping, as is shown in Fig.13 for  $^{22}\text{O}$ . This calculation is done with use of the discretized continuum quasiparticle states obtained with the box boundary condition (the box radius  $r_{max} = 20$  fm), instead of using the exact Green function with the out-going boundary condition adopted in the present continuum calculations. In the discretized calculation there are several discrete peaks in the energy region of the soft dipole excitation. The four major peaks seen in the interval  $E = 5 - 9 \text{ MeV}$  have different behaviors in the transition densities while the transition densities in the continuum calculation varies smoothly as a function of the excitation energy. The soft dipole excitation cannot be represented by one of these discrete peaks.

The E1 strength in the soft dipole region is experimentally measured in neutron rich oxygen isotopes, and the energy weighted sum of the E1 strength below  $E < 15 \text{ MeV}$  is extracted[9]. We evaluate the corresponding energy weighted sum from the calculated strength function, and list in Table II. The experimental value of the energy weighted sum is about 8% of the Thomas-Reiche-Kuhn sum rule value in  $^{18,22}\text{O}$ , and about 12% in  $^{20}\text{O}$ [9]. The calculation gives a fair agreement with the experimental data in  $^{18,20}\text{O}$ , but it overestimates in  $^{22}\text{O}$ . The agreement may be improved by refining the model Hamiltonian, e.g., the Woods-Saxon parameters, or by adopting a selfconsistent Hartree-Fock potential which is expected to be more realistic. Note that the shell model[25] and the phonon coupling model[26] based on the Skyrme HF+BCS+QRPA approach exhibit a saturation around  $^{22}\text{O}$ .

Comparing among O, Ca, and Ni isotopic chains, we observe slightly different behaviors in the soft dipole excitation. In the case of Ni isotopes, the E1 strength is distributed at very low excitation energy as the neutron threshold energy is very low ( $E_{th,1} \sim 0.70 - 2.45 \text{ MeV}$ ). This can be related to the small neutron Fermi energy in the  $A = 80 - 86$  nickel isotopes, which is only about  $-1.50 \sim -0.40 \text{ MeV}$ . Note also that the single-particle energies of the most weakly bound neutron Woods-Saxon orbits  $3s_{1/2}$  and  $2d_{5/2}$  in the vicinity of the Fermi energy are small;  $e_{3s_{1/2}, 2d_{5/2}} \sim -1 \text{ MeV}$  (Fig.1). In Ca isotopes, the increase of the E1 strength above the neutron threshold energy  $E_{th,1}$  is not as steep as in O and Ni, but instead a small peak is formed at the energy which slightly deviates from the threshold energy. This is because there is no weakly bound neutron  $s$  orbit in the calcium isotopes while  $p$  orbits ( $2p_{1/2,3/2}$ ) participate instead (see the following section for details).

### C. Pairing effects on dipole strength

We analyze effects of the neutron pair correlation on the soft dipole excitation, which is the primary issue in the present investigations. To visualize the influence of neutron pairing correlation, we perform a calculation where the neutron pairing interaction is switched off, i.e. by setting  $V_0 = 0$ . (For open sub-shell nuclei such as  $^{18,20}\text{O}$  a very weak pairing interaction  $V_0 = -28 \text{ MeVfm}^3$  is used to guarantee a  $J^\pi = 0^+$  configuration in the last  $j$ -shell orbit partially occupied in the ground state. This choice produces a so small average pairing gap  $\langle\Delta_n\rangle < 0.1 \text{ MeV}$  that the pair correlation effects are negligible.) Calculated results are shown by the dotted line in Fig.12. We immediately see a sizable pairing effect on the E1 strength of the soft dipole excitation whereas there is essentially no effect on the giant dipole resonance. To focus on the soft dipole excitation, we show a magnified portion of the dipole strength function in Fig.14.

It is seen that the effect of neutron pairing correlation on the soft dipole strength varies depending on the isotopic chains and mass numbers. *i) In the oxygen isotopes*, the neutron pairing correlation increases significantly the E1 strength in the soft dipole region in  $^{20,22}\text{O}$  (and slightly less clearly in  $^{18}\text{O}$ ). Table II lists the  $B(\text{E1})$  value of the soft dipole excitation integrated over an energy window of 4MeV width above the one neutron threshold energy  $E_{th,1}$ . The pairing correlation increases the  $B(\text{E1})$  value by about 50-80 % in  $^{18-22}\text{O}$ . The energy weighted sum of  $B(\text{E1})$  up to  $E = 15 \text{ MeV}$  is also tabulated in Table II. Influence of pairing on the energy weighted sum is relatively small in comparison with that on the  $B(\text{E1})$  value. This is because the pairing effect becomes weaker at higher excitation energies. The pairing effect is negligible in the case of  $^{24}\text{O}$ , but this is because the pair correlation itself is very small ( $\langle\Delta_n\rangle = 0.66 \text{ MeV}$ ) in this nucleus. *ii) In the calcium isotopes*, the pairing correlation does not enhance the magnitude of E1 strength. Instead it shifts the low-lying dipole strength up in the excitation energy and/or it suppresses the strength of the soft dipole excitation. The suppression in the E1 strength is about 20% in  $^{54}\text{Ca}$  (see Table III). *iii) In the nickel isotopes*, the neutron pair correlation either suppresses significantly the E1 strength at low energies (in  $^{86}\text{Ni}$  by about 30%, see Table III) or modifies the shape of strength distribution (in  $^{80-84}\text{Ni}$ , see Fig.14). After all, the pair correlation certainly influences the strength distribution of the soft dipole excitation, but it can either enhance (as in the case of  $^{20,22}\text{O}$ ) or suppress (as in  $^{54}\text{Ca}, ^{86}\text{Ni}$ ) the E1 strength.

To analyze the pair correlation effect, it is useful to decompose it into the *static* and the *dynamical* mechanisms[28, 34]. Note that the pair correlation changes the static mean-fields in the HFB Hamiltonian, in particular the pair potential  $\Delta(\mathbf{r})$ . This mean-field effect modifies the ground state configuration and the single-particle excitation, through which the excitation properties are also affected. We call this mechanism *the static pair correlation effect*. On the other hand, the RPA correlation associated with the dynamical variation in the pair potential  $\delta\Delta(r\omega)$  gives the additional pair correlation effect on the excitation, which we call *the dynamical pair correlation effect*. In other words, the dynamical pair correlation effect originates from the residual interaction taken into account in the RPA equation (9), while the static effect are present even in the unperturbed response. To examine these pair correlation effects separately, we have performed calculations where the dynamical pair correlation is neglected while keeping the static pairing effects. Result is shown in Fig.14 with the dashed line. It is immediately seen that both the static and the dynamical correlations give considerable effects on the dipole strength in the soft excitation region.

Let us first focus on *the static pairing effect*. It is seen that the static effect is a major part of the net pairing effect on the dipole strength, and produces qualitative trends of the strength function, although the dynamical effect cannot be neglected for quantitative description. To get more insight to the static effect, we look into the unperturbed strength function which is obtained by neglecting all the residual interactions(Fig.15). In the unperturbed strength, we separate contributions from different two-quasiparticle excitations by selecting a specified pair of angular momenta of the two-quasiparticle configurations. Taking  $^{22}\text{O}$  as an example, where the pairing effect on the soft dipole excitation is large, we find that the static pairing effect increases the unperturbed E1 strength. This arises mainly from a contribution of a neutron two-quasiparticle configuration exciting the  $2s_{1/2}$  state and the continuum  $p$  states coupled to  $L = 1$ , abbreviated as  $[2s_{1/2} \times p^*]_{L=1}$  or more shortly  $2s_{1/2} \times p^*$  (the asterisk denotes the continuum states), as seen from comparison between the left top and the left bottom panels of Fig.15. This quasiparticle excitation is available only by taking into account the ground state pair correlation. This is because the Woods-Saxon  $2s_{1/2}$  orbit located above the Fermi energy (Fig.1) can be partially occupied only if the pair correlation is included. The contribution of the  $2s_{1/2} \times p^*$  configuration to the dipole strength is added with those of  $1d_{5/2} \times p^*$  configurations, which are dominant ones when the pairing is neglected (see the lower panel of Fig.15). In  $^{18-20}\text{O}$ , the increase of dipole strength due to the static pairing effect is similarly seen, but it not very large since the occupation of the  $2s_{1/2}$  orbit is smaller. Another aspect of the static pairing effect is that it pushes up the strength to slightly higher energy. This is because the pair correlation increases the energy of the two-quasiparticle excitation than that of the corresponding unpaired particle-hole excitation.

The static pairing effect in Ca and Ni isotopes appears different from that in the oxygen isotopes. For example, it causes the large suppression of the E1 strength in  $^{86}\text{Ni}$ , which is explained in terms of the neutron  $3s_{1/2}$  orbit. This orbit would be fully occupied by the last two neutrons if we neglected the pair correlation (cf. Fig.1). Since the

$3s_{1/2}$  orbit is only weakly bound (the Woods-Saxon single-particle energy  $e_{2s_{1/2}} = -0.78$  MeV) and has an spatially extended wave function, the particle-hole excitations from this orbit to the continuum  $p$  orbits bring about a large E1 strength just above the one-neutron threshold energy, which is often referred to as the threshold strength (cf. the right lower panel of Fig.15). Once the neutron pair correlation is included, the associated strength is reduced as the  $3s_{1/2}$  orbit becomes partially occupied, making the contribution of the two-quasiparticle configurations  $3s_{1/2} \times p^*$  to the dipole strength significantly smaller. In Ca isotopes, the unperturbed strength in the soft dipole strength is dominated by contributions of the two-quasiparticle excitations  $2p_{1/2,3/2} \times d^*$  and  $2p_{1/2,3/2} \times s^*$  (Fig.15). The increase in the quasiparticle energy of the  $2p_{1/2,3/2}$  state caused by the pair correlation pushes up the peak around  $E \sim 7$  MeV by about 1MeV.

We thus conclude that the static pairing effect shows variety in different nuclides, depending strongly on low-energy quasiparticle states (around the Fermi energy) which are quite sensitive to the pairing correlation.

We then look into *the dynamical pairing effect*. We immediately see that, in contrast to the static effect, the dynamical pairing effect has a systematic tendency to increase the dipole strength in all examples shown in Fig.14 although the magnitude of the increase varies. The effect on  $B(E1)$  associated with the soft dipole excitation is shown in Tables II and III. The largest effect on  $B(E1)$  amounting to 10 – 40% is seen in  $^{18-22}\text{O}$ , and  $\sim 10 - 15\%$  in the nickel isotopes. The increase of the strength due to the dynamical pairing effect is found in the previous QRPA calculations for oxygen isotopes[29, 34, 42]. We here find that the increase due to the dynamical pairing correlation is universally seen in spherical nuclei near drip-line in the medium mass region. Note also that the enhancement due to the dynamical pairing effect has a similarity to the pair interaction effect predicted on the soft dipole excitation in the two-neutron halo nucleus  $^{11}\text{Li}$ [14].

#### D. Transition densities: particle-particle dominance in the soft dipole excitation

Characters of the soft dipole excitation can be clarified more directly by looking into the transition densities. Choosing a representative energy, we evaluate the particle-hole transition density  $\rho^{ph}(r)$ , the particle-pair and the hole-pair transition densities  $P^{pp}(r)$  and  $P^{hh}(r)$ . They are plotted in Figs.16, 17 and 18. It is seen in the particle-hole transition density  $\rho^{ph}(r)$  that in the external region ( $r \gtrsim R_{surf}$ ) the soft dipole excitation has significant neutron amplitude whereas there is essentially no amplitude for protons, indicating that only neutrons are moving in the external region. At and slightly inside the surface, the particle-hole amplitudes of neutrons and protons have the same sign, but with the opposite phase to the external neutron amplitude, indicating that both neutrons and protons in this region move coherently against the external neutron motion. The external neutron motion is responsible for the soft dipole strength. This behavior of the particle-hole transition density in the soft dipole excitation is commonly seen also in other RPA and QRPA calculations without and with the pair correlations[22, 23, 24, 28, 29].

A novel finding in the present analysis is that the neutron particle-pair transition density  $P^{pp}(r)$  has very large amplitude in the external region, where the amplitude even exceeds that of the particle-hole transition density  $\rho^{ph}(r)$ . The hole-pair transition density  $P^{hh}(r)$  on the other hand is the smallest among the three transition densities, and almost negligible in the external region. The relation  $|P^{pp}(r)| > |\rho^{ph}(r)| > |P^{hh}(r)|$  in the external region is seen in all isotopes in Figs.16, 17 and 18, except in  $^{24}\text{O}$  and  $^{58}\text{Ca}$ , where  $P^{pp}(r)$  is still sizable. The dominance of  $P^{pp}(r)$  indicates that the soft dipole excitation has a character of a particle-particle excitation: It is more appropriate to characterize the soft dipole excitation as a motion of spin-singlet neutron pair in the external region, than to describe as a simple particle-hole excitation of a neutron to continuum states. We also note that the particle-pair transition density  $P^{pp}(r)$  displays a characteristic isotopic dependence. The large particle-pair amplitude in  $^{50,54}\text{Ca}$  and  $^{18-22}\text{O}$  decreases with increasing the neutron number, while the particle-hole amplitude increases in the other way. A similar but slightly weak isotopic dependence is seen in the nickel isotopes.

In order to reveal origin of the particle-particle dominance in the soft dipole excitation, we investigate influence of the pairing correlations on the transition densities. Comparing with calculations where the pairing effects are fully neglected (shown in Figs.16, 17 and 18 by the dotted line), we immediately see that the neutron pair correlation brings about the large particle-pair amplitude in the exterior region  $r > R_{surf}$ . In Figs.16, 17 and 18 we show also results obtained by neglecting the dynamical pairing correlation. It is seen that both the static and the dynamical pair correlations are responsible for the particle-particle dominance. In particular, the dynamical pair correlation has a dramatic influence to enhance  $P^{pp}(r)$  by a factor of about two or more in the external region. In the following we shall investigate in more detail the static and the dynamical effects separately.

*i) The static pairing effect:* Generally low energy two-quasiparticle excitations, which are building blocks of low-lying excitations under the influence of pairing correlation, carry simultaneously particle-hole, particle-pair and hole-pair amplitudes. On the contrary, only the particle-hole amplitude would exist if the static pairing correlation were absent in the case of  $j$ -shell closed nuclei. As an example, let us consider the neutron two-quasiparticle excitations  $2s_{1/2} \times p^*$  and  $1d_{5/2} \times p^*$  (and  $1d_{5/2} \times f^*$ ), which give dominant contributions to unperturbed strength function in  $^{22}\text{O}$  (cf. Fig.15).

We first note that the two-quasiparticle configuration  $2s_{1/2} \times p^*$  would never participate in the soft dipole excitation if the pairing correlation were absent. With the pairing correlation included, the quasiparticle state  $2s_{1/2}$  has a large amplitude both in the upper and lower components (corresponding to the particle and hole components, respectively) of the wave function since it is located near the Fermi energy. Accordingly the two-quasiparticle configuration  $2s_{1/2} \times p^*$  brings a large amplitude both in the particle-hole transition density  $\rho^{ph}(r)$  and in the particle-pair transition density  $P^{pp}(r)$ . (The hole-pair transition density  $P^{hh}(r)$  is small since both  $2s_{1/2}$  and  $p^*$  are located above the Fermi energy, and particle characters are dominant in these quasiparticle states.) The amplitudes  $P^{pp}(r)$  and  $\rho^{ph}(r)$  associated with the configuration  $2s_{1/2} \times p^*$  is especially large in the exterior region as the quasiparticle wave function of the  $2s_{1/2}$  state is spatially extended to the outside. The other dominant configuration  $1d_{5/2} \times p^*(f^*)$  contributes also to the particle-pair transition density in a similar way. The nodal pattern of the transition densities is consistent with the mixture of these two-quasiparticle configurations. The particle-particle character of these two-quasiparticle excitations in  $^{18,20}\text{O}$  decreases as the Fermi energy (the neutron number) increases. In  $^{24}\text{O}$ , the particle-particle character becomes small as the quasiparticle states  $1d_{5/2}$  and  $2s_{1/2}$  both have a dominant hole character. The qualitative trends observed in the transition densities can be connected in this way to the properties of the relevant quasiparticle states. Similar mechanism are applied to the calcium isotopes, where the neutron  $2p_{3/2,1/2}$  states play a central role. In the nickel isotopes, the relevant neutron quasiparticle states are  $3s_{1/2}$  and  $2d_{5/2}$  (see Figs.1 and 15).

*ii) The dynamical pairing effect:* It is clear that the static pairing effects discussed above explains only qualitative aspects of the transition densities since the static pairing effect alone explains about a half of the particle-pair transition amplitude. The dynamical effect adds an essential enhancement in  $P^{pp}(r)$  especially in the external region which is most relevant to the soft dipole excitation. The increase by a factor of 2 in the particle-pair transition amplitude  $P^{pp}(r)$  corresponds to an enhancement of a factor of about four in the strength of neutron pair transfer. Namely the characteristic particle-pair dominance of the soft excitation is strongly affected by the RPA correlations. This means that the calculated soft dipole excitation cannot be explained as a few representative two-quasiparticle configurations which we find responsible for the static pairing effect, such as  $2s_{1/2} \times p^*$  or  $1d_{5/2} \times p^*(f^*)$  in the case of O isotopes, This conclusion is quite different from that of the RPA calculations neglecting the pair correlations[22, 24], which predict the soft dipole excitation in neutron-rich oxygen isotopes as a non-collective independent particle-hole excitation of weakly bound neutrons.

### E. Di-neutron correlation in the soft dipole excitation

We shall investigate nature of the large dynamical pairing effect on the particle-pair transition density  $P^{pp}(r)$ . The large amplitude in  $P^{pp}(r)$  itself indicates that the pair correlation enhances the probability to find two neutrons participating in the soft dipole excitation at the same position  $\mathbf{r}$ . It is then tempting to interpret it in connection with the di-neutron correlation which we found in the ground state. To check this viewpoint, we examine contributions of high- $l$  quasiparticle orbits to the soft dipole excitations.

We have performed calculations where contribution of quasiparticles with high angular momenta is truncated in evaluating the RPA correlations. In practice, we put an upper cut-off  $l_{cut}$  to the sum over orbital angular momenta  $l$  and  $l'$  of the two quasiparticle configurations in the density response function, Eq.(15). If the pairing correlation is completely neglected, the angular momentum of quasiparticles contributing to the dipole response is limited in a small range  $0 \leq l \leq l_{cut}^0 = l_{occ} + 1$ , where  $l_{occ}$  is the largest orbital angular momenta of the occupied bound Woods-Saxon single-particle orbits. In the case of oxygen isotopes  $^{18-24}\text{O}$ , for instance, neutrons would occupy  $s, p$  and  $d$  bound orbits in the ground state in the null pairing case, and hence only the angular momentum combinations  $[s \times p]_{L=1}$ ,  $[p \times d]_{L=1}$  and  $[d \times f]_{L=1}$  contribute. The cut-off  $l_{cut}^0 = 3$  is sufficient in this case. As the pairing correlation is taken into account, however, all combinations including  $[l \times (l+1)]_{L=1}$  with  $l \geq l_{cut}^0$  are allowed to contribute. Note that these high- $l$  quasiparticle states are all continuum orbits.

Results of the truncated calculations are shown in Fig.19. It is seen that contributions from neutron high- $l$  quasiparticle states with  $l > l_{occ}$  are essential to produce the large enhancement in the particle-particle transition density. In  $^{22}\text{O}$  and  $^{54}\text{Ca}$ , the angular momenta up to  $l \sim 9$  and  $l \sim 10$  respectively are necessary to approach the final result. In  $^{84}\text{Ni}$ , the orbits up to  $l \sim 13$  contribute in the external region up to  $r \lesssim 12$  fm, but very high angular momenta  $l > 13$  still continue to influence in the far outside  $r \gtrsim 15$  fm. The particle-hole transition amplitude  $\rho^{ph}(r)$ , on the other hand, is affected very little by the high- $l$  continuum configurations with  $l > l_{occ}$ , as seen in Fig.19.

We thus conclude that the neutron correlation responsible for the large enhancement of the particle-pair transition density  $P^{pp}(r)$  in the soft dipole excitation is associated with a coherent superposition of a large number of neutron two-quasiparticle configurations with angular momentum coupling  $[l \times (l+1)]_{L=1}$  involving up to large values of  $l$ . The accumulating high- $l$  contribution can be viewed as an evidence that two neutrons carrying the soft dipole mode are spatially correlated at short relative distance in such a way that we have seen the di-neutron correlation in the ground state (cf. Section II C). This suggests that the soft dipole excitation is characterized rather strongly by motion

of a spin-singlet di-neutron in the nuclear exterior against the remaining  $A - 2$  system.

It is noted that much larger values of angular momentum contribute in the soft dipole excitation than in the ground state. In  $^{84}\text{Ni}$ , for example, we need angular momentum up to  $l \sim 13$  to achieve an approximate convergence around  $r = 7 - 12$  fm where the pair transition density has the dominant distribution. This is because the di-correlation correlation in the soft dipole excitation takes place in much far outside of the nuclear surface than that in the case of the ground state. Note also that in  $^{84}\text{Ni}$  convergence of high- $l$  contributions to the particle-pair transition density  $P^{pp}(r)$  is slow in the very far exterior  $r > 15$  fm even around the maximum angular momentum  $13 \lesssim l \leq l_{max}(= 17)$ . This is related to the fact that two neutrons can escape simultaneously in the nickel isotopes where the soft dipole mode lies above the two neutron threshold energy  $E_{th,2}$ . The oscillation of  $P^{pp}(r)$  at  $r \gtrsim 10$  fm indeed indicates a sizable two-neutron escaping. The slow convergence with respect to the angular momentum at very large distances suggests that there exists the pair correlation between the two escaping neutrons.

## F. Dependence on pair interaction

Since the soft dipole excitation is strongly influenced by the neutron pairing correlation, sensitivity of the soft dipole excitation to the effective pairing force is expected. We shall examine this issue in connection with the di-neutron correlation.

We have performed an analysis to see dependence on the force strength  $V_0$  for  $^{22}\text{O}$  taken as an representative example. We increase the strength  $|V_0|$  of the mixed pairing force from the reference value  $V_0 = -280 \text{ MeVfm}^3$  (corresponding to  $\langle \Delta_n \rangle = 1.5 \text{ MeV}$  fitted to the experimental odd-even mass difference) to  $V_0 = -350 \text{ MeVfm}^3$  ( $\langle \Delta_n \rangle = 2.8 \text{ MeV}$  representing the conventional systematics  $\Delta_{sys} = 12/\sqrt{A} \text{ MeV}$ ), as is done in Section II. The calculated E1 strength function and the particle-pair transition density are compared in Fig.20. As expected, the increase of  $V_0$  modifies the strength distribution of the soft dipole excitation: The dipole strength calculated with  $V_0 = -350 \text{ MeVfm}^3$  is larger than that with  $V_0 = -280 \text{ MeVfm}^3$ . As seen in the right panel of the Fig.20, the increase is caused essentially by the dynamical pairing correlation. More dramatic sensitivity is recognized in the particle-pair transition density  $P^{pp}(r)$ , on which the dynamical pairing effect becomes significantly larger with increasing  $V_0$ . These observations are consistent with the picture that the di-neutron correlation manifests itself in the soft dipole excitation. It is also in accord with the finding in the previous section that the increase of  $V_0$  enhances the di-neutron correlation in the ground state (See. Section IID and Fig.9).

We have also examined sensitivity to the density dependence of the pairing force. To this end, we performed calculations with use of the volume pairing (the density independent) force, and the surface pairing force with strong density dependence as is done in Section II. Calculated results are shown in Figs.21 and 22, which may be compared also with those using the mixed pairing force, representing an intermediate density dependent force (cf. Figs.14, 16, 17 and 18). Figs.21 and 22 clearly show that results are very different with different density dependences. It is seen that the dynamical enhancement of the particle-pair transition density  $P^{pp}(r)$  in the external region ( $r > R_{surf}$ ) is much larger with the surface pairing force than with the mixed and the volume pairing forces (Fig.22). This trend is also seen in the E1 strength (Fig.21). In the case of the volume pairing force, on the other hand, the dynamical pairing effect on the strength function becomes almost insignificant, and even the particle-pair transition density is not strongly enhanced.

Note that the neutron-neutron attraction acting in the low-density external region is proportional to the value of  $V_0$ , which differs as  $|V_0| \approx 180, 280, 380 \text{ MeVfm}^3$  for the volume, the mixed, and the surface pairing forces, respectively. Thus the above observation implies that the soft dipole excitation, especially the associated particle-pair transition density, is quite sensitive to the effective pairing force among neutrons moving in the low-density part outside the nuclear surface. This is of course related to the fact that the soft dipole excitation is essentially a mode carried by the correlated neutrons moving in the nuclear exterior. In addition, the strong sensitivity to the density dependence is in accord with a similar behavior of the di-neutron correlation in the ground state (cf. Fig.10). This again supports the picture that the soft dipole excitation is strongly influenced by the neutron pairing correlation of the di-neutron type.

## IV. CONCLUSIONS

We have investigated the neutron pairing correlations and their influences on the soft dipole excitation in medium mass nuclei near neutron drip-line from the viewpoint of the di-neutron correlation.

The analysis using the two-body correlation density has revealed the presence of spatial di-neutron correlation in the pair correlated ground state in nuclei near drip-line. It is found that correlated neutron pairs exhibit a strong concentration of the probability of about 30-60% at short relative distances  $|\mathbf{r} - \mathbf{r}'| \lesssim 2 \text{ fm}$ , which is much smaller than the nuclear radius. This di-neutron correlation enhances in the surface and the skin regions in near-drip-line nuclei

although it also exists inside the nucleus and also in stable nuclei along the isotopic chain. The di-neutron correlation originates from coherent superposition of the single-particle (quasiparticle) orbits with large orbital angular momenta, which are embedded in the continuum energy region.

We have analyzed the soft dipole excitation to search for the di-neutron correlation in this mode. It is found that the particle-pair transition density of neutrons in the soft dipole excitation is quite large outside the nuclear surface. This originates from the dynamical pairing correlation among neutrons moving in the external region, i.e., the RPA correlation for the excited state caused by the pairing interaction. Indeed the dynamical pair correlation is responsible for enhancing the particle-pair transition density by a factor of about two or more. This indicates that the soft dipole excitation under the influence of neutron pairing correlation has a dominant particle-particle character, rather than an uncorrelated particle-hole excitation from a weakly orbit to continuum orbits. We find also that two-quasiparticle configurations  $[l \times (l + 1)]_{L=1}$  involving continuum high- $l$  orbits up to around  $l \sim 10$  accumulate coherently to bring about the large particle-pair transition density. This strongly suggests that there is the di-neutron correlation among neutrons participating in the soft dipole excitation. We are thus lead to a picture that in the soft dipole excitation a spin-singlet di-neutron move outside the nucleus against the  $A - 2$  subsystem. Our analysis reveals also that the characteristic neutron pairing effects are sensitive to the density dependence of the effective pairing force. The influence of neutron pairing correlation on the dipole strength is sizable, but not always causes enhancement. The di-neutron correlation emerges more clearly in the particle-particle channel.

We expect that the di-neutron correlation present in the soft dipole excitation may be most easily and directly probed in the two-particle correlation among two neutrons escaping from the excited state, or in transfer of neutrons to the excited state. These processes may also be used as a probe to study the density dependence of the nuclear pairing correlations. These issues are interesting subjects for future investigations.

### Acknowledgments

The authors thank K. Matsuyanagi, W. Nazarewicz, F. Barranco, E. Vigezzi, G. Gori, N. Sandulescu for valuable discussions. They also thank discussions with the members of the Japan-U.S. Cooperative Science Program “Mean-Field Approach to Collective Excitations in Unstable Medium-Mass and Heavy Nuclei”. The numerical calculations were performed on the NEC SX-5 supercomputer systems at Research Center for Nuclear Physics, Osaka University and at Yukawa Institute for Theoretical Physics, Kyoto University. This work was supported by the Grant-in-Aid for Scientific Research (No. 14540250) from the Japan Society for the Promotion of Science.

- 
- [1] D. Sackett, K. Ieki, A. Galonsky, C. A. Bertulani, H. Esbensen, J. J. Kruse, W. G. Lynch, D. J. Morrissey, N. A. Orr, B. M. Sherrill, H. Schulz, A. Sustich, J. A. Winger, F. Deák, Á. Horváth, and Á. Kiss, Z. Seres, J. J. Kolata, R. E. Warner, D. L. Humphrey, *Phys. Rev. C* **48**, 118 (1993).
  - [2] S. Shimoura, T. Nakamura, M. Ishihara, N. Inabe, T. Kobayashi, T. Kubo, R. H. Siemssen, I. Tanihata and Y. Watanabe, *Phys. Lett.* **B348**, 29 (1995).
  - [3] M. Zinser, F. Humbert, T. Nilsson, W. Schwab, H. Simon, T. Aumann, M. J. G. Borge, L. V. Chulkov, J. Cub, Th. W. Elze, H. Emling, H. Geissel, D. Guillemaud-Mueller, P. G. Hansen, R. Holzmann, H. Irnich, B. Jonson, J. V. Kratz, R. Kulesa, Y. Leifels, H. Lenske, A. Magel, A. C. Mueller, G. Münzenberg, F. Nickel, G. Nyman, A. Richter, K. Riisager, C. Scheidenberger, G. Schrieder, K. Stelzer, J. Stroth, A. Surowiec, O. Tengblad, E. Wajda, E. Zude, *Nucl. Phys.* **A619**, 151 (1997).
  - [4] T. Nakamura, S. Shimoura, T. Kobayashi, T. Teranishi, K. Abe, N. Aoi, Y. Doki, M. Fujimaki, N. Inabe, M. Iwasa, K. Katori, T. Kubo, H. Okuno, T. Suzuki, I. Tanihata, Y. Watanabe, A. Yoshida, M. Ishihara, *Phys. Lett.* **B331**, 296 (1994).
  - [5] R. Palit, P. Adrich, T. Aumann, K. Boretzky, B. V. Carlson, D. Cortina, U. Datta Pramanik, Th. W. Elze, H. Emling, H. Geissel, M. Hellström, K. L. Jones, J. V. Kratz, R. Kulesa, Y. Leifels, A. Leistenschneider, G. Münzenberg, C. Nociforo, P. Reiter, H. Simon, K. Sümmerer, and W. Walus, *Phys. Rev. C* **68**, 034318 (2003).
  - [6] T. Nakamura, N. Fukuda, T. Kobayashi, N. Aoi, H. Iwasaki, T. Kubo, A. Mengoni, M. Notani, H. Otsu, H. Sakurai, S. Shimoura, T. Teranishi, Y. X. Watanabe, K. Yoneda, and M. Ishihara, *Phys. Rev. Lett.* **83**, 1112 (1999).
  - [7] U. Datta Pramanik, T. Aumann, K. Boretzky, B. V. Carlson, D. Cortina, Th. W. Elze, H. Emling, H. Geissel, A. Grünschloß, M. Hellström, S. Ilievski, J. V. Kratz, R. Kulesa, Y. Leifels, A. Leistenschneider, E. Lubkiewicz, G. Münzenberg, P. Reiter, H. Simon, K. Sümmerer, E. Wajda and W. Walus *Phys. Lett.* **B551**, 63 (2003).
  - [8] T. Aumann, D. Aleksandrov, L. Axelsson, T. Baumann, M. J. G. Borge, L. V. Chulkov, J. Cub, W. Dostal, B. Eberlein, Th. W. Elze, H. Emling, H. Geissel, V. Z. Goldberg, M. Golovkov, A. Grünschloß, M. Hellström, K. Hencken, J. Holeczek, R. Holzmann, B. Jonson, A. A. Korshenninikov, J. V. Kratz, G. Kraus, R. Kulesa, Y. Leifels, A. Leistenschneider, T. Leth, I. Mukha, G. Münzenberg, F. Nickel, T. Nilsson, G. Nyman, B. Petersen, M. Pfützner, A. Richter, K. Riisager,

- C. Scheidenberger, G. Schrieder, W. Schwab, H. Simon, M. H. Smedberg, M. Steiner, J. Stroth, A. Surowiec, T. Suzuki, O. Tengblad, and M. V. Zhukov, Phys. Rev. C **59**, 1252 (1999).
- [9] A. Leistenschneider, T. Aumann, K. Boretzky, D. Cortina, J. Cub, U. Datta Pramanik, W. Dostal, Th. W. Elze, H. Emling, H. Geissel, A. Grünschloß, M. Hellström, R. Holzmann, S. Ilievski, N. Iwasa, M. Kaspar, A. Kleinböhl, J. V. Kratz, R. Kulesa, Y. Leifels, E. Lubkiewicz, G. Münzenberg, P. Reiter, M. Rejmund, C. Scheidenberger, C. Schlegel, H. Simon, J. Stroth, K. Sümmerner, E. Wajda, W. Walús, and S. Wan Phys. Rev. Lett. **86**, 5442 (2001).
- [10] E. Tryggestad, T. Baumann, P. Heckman, and M. Thoennessen, T. Aumann, D. Bazin, Y. Blumenfeld, J. R. Beene, T. A. Lewis, D. C. Radford, D. Shapira, R. L. Varner, M. Chartier, M. L. Halbert, J. F. Liang, Phys. Rev. C **67**, 064309 (2003).
- [11] A. Ozawa, O. Bochkarev, L. Chulkov, D. Cortina, H. Geissel, M. Hellström, M. Ivanov, R. Janik, K. Kimura, T. Kobayashi, A. A. Korshennikov, G. Münzenberg, F. Nickel, Y. Ogawa, A. A. Ogloblin, M. Pfützner, V. Pribora, H. Simon, B. Sitár, P. Strmend, K. Sümmerner, T. Suzuki, I. Tanihata, M. Winkler, K. Yoshida, Nucl. Phys. **A691**, 599 (2001).
- [12] H. Sagawa, N. Van Giai, N. Takigawa, M. Ishihara, K. Yazaki, Z. Phys. **A351**, 385 (1995).
- [13] F. Catara, C. H. Dasso, A. Vitturi, Nucl. Phys. **A602**, 181 (1996).
- [14] G. F. Bertsch, H. Esbensen, Ann. Phys. **209**, 327 (1991).  
H. Esbensen, G. F. Bertsch, Nucl. Phys. **A542**, 310 (1992).
- [15] K. Ikeda, INS Report JHP-7 (1988); Nucl. Phys. **A538**, 355c (1992).
- [16] M. V. Zhukov, B. V. Danilin, D. V. Fedorov, J. M. Bang, I. J. Thompson, J. S. Vaagen, Phys. Rep. **231**, 151 (1993).
- [17] F. Barranco, P. F. Bortignon, R. A. Broglia, G. Coló, E. Vigezzi, Eur. Phys. J. **A11**, 385 (2001).
- [18] S. Aoyama, K. Katō, K. Ikeda, Prog. Theor. Phys. Suppl. **142**, 35 (2001).  
T. Myo, S. Aoyama, K. Katō, K. Ikeda, Prog. Theor. Phys. **108**, 133 (2002).
- [19] P. G. Hansen, B. Jonson, Europhys. Lett. **4**, 409 (1987).
- [20] B. V. Danilin, I. J. Thompson, J. S. Vaagen, M. V. Zhukov, Nucl. Phys. **A632**, 383 (1998).
- [21] The collective vibrational mode of halo neutrons predicted by Ref.[15] is called the soft dipole mode or the soft dipole resonance. The term soft dipole excitation, on the other hand, is sometime used to distinguish from this picture or to emphasize a picture of uncorrelated excitation of halo neutrons. In the present paper, however, we use the soft dipole excitation only to imply neutrally an excitation carrying a significant E1 strength far below the giant dipole resonance energy without specifying any other characters.
- [22] F. Catara, E. G. Lanza, M. A. Nagarajan, A. Vitturi, Nucl. Phys. **A624**, 449 (1997).
- [23] I. Hamamoto, H. Sagawa, X. Z. Zhang, Phys. Rev. C **57** (1998), R1064; Nucl. Phys. **A648**, 203 (1999).
- [24] D. Vretenar, N. Paar, P. Ring, G. A. Lalazissis, Nucl. Phys. **A692**, 496 (2001).
- [25] H. Sagawa, T. Suzuki, Phys. Rev. C **59**, 3116 (1999).
- [26] G. Colò, P. F. Bortignon, Nucl. Phys. **A696**, 427 (2001).
- [27] S. Goriely, E. Khan, Nucl. Phys. **A706**, 217 (2002).
- [28] M. Matsuo, Prog. Theor. Phys. Suppl. **146**, 110 (2002).
- [29] N. Paar, P. Ring, T. Niksic, D. Vretenar, Phys. Rev. C **67**, 034312 (2003).
- [30] J. Dobaczewski, H. Flocard, J. Treiner, Nucl. Phys. **A422**, 103 (1984).
- [31] J. Dobaczewski, W. Nazarewicz, T. R. Werner, J. F. Berger, C. R. Chinn, J. Dechargé, Phys. Rev. C **53**, 2809 (1996).
- [32] A. Bulgac, preprint FT-194-1980, nucl-th/9907088.
- [33] P. Ring, P. Schuck, *The Nuclear Many-Body Problem*, (Springer-Verlag, 1980).
- [34] M. Matsuo, Nucl. Phys. **A696**, 371 (2001).
- [35] S. Shlomo, G. Bertsch, Nucl. Phys. **A243**, 507 (1975).
- [36] G. F. Bertsch, S. F. Tsai, Phys. Rep. **18**, 125 (1975).
- [37] G. A. Bartholomew, E. D. Earle, A. J. Ferguson, J. W. Knowles, M. A. Lone, Adv. Nucl. Phys. **7**, 229 (1972).
- [38] M. Igashira, H. Kitazawa, M. Shimizu, H. Komano, Y. Yamamuro, Nucl. Phys. **A457**, 301 (1986).
- [39] Y. Suzuki, K. Ikeda, H. Sato, Prog. Theor. Phys. **83**, 180 (1987).
- [40] D. Vretenar, N. Paar, P. Ring, G. A. Lalazissis, Phys. Rev. C **63**, 047301 (2001).
- [41] N. Ryezayeva, T. Hartmann, Y. Kalmykov, H. Lenske, P. von Neumann-Cosel, V. Yu. Ponomarev, A. Richter, A. Shevchenko, S. Volz, J. Wambach, Phys. Rev. Lett. **89**, 272502 (2002).
- [42] M. Matsuo, Proc. Int. Symp. on Frontiers of Collective Motions, eds. H. Sagawa and H. Iwasaki (World Scientific 2003) p.312.  
M. Matsuo, Proc. Int. Symp. "A New Era of Nuclear Structure Physics", eds. Y. Suzuki, S. Ohya, M. Matsuo, T. Ohtsubo (World Scientific 2004).
- [43] R. R. Chasman, Phys. Rev. C **14**, 1935 (1976).
- [44] J. Terasaki, P.-H. Heenen, P. Bonche, J. Dobaczewski, H. Flocard, Nucl. Phys. **A593**, 1 (1995).
- [45] E. Garrido, P. Sarriguren, E. Moya de Guerra, P. Schuck, Phys. Rev. C **60**, 064312 (1999).
- [46] J. Dobaczewski, W. Nazarewicz, P.-G. Reinhard, Nucl. Phys. **A693**, 361 (2001).
- [47] J. Dobaczewski, W. Nazarewicz, Prog. Theor. Phys. Suppl. **146**, 70 (2002).  
J. Dobaczewski, W. Nazarewicz, M. V. Stoitsov, Euro. Phys. J. **A15**, 21 (2002).
- [48] W. Satuła, J. Dobaczewski, W. Nazarewicz, Phys. Rev. Lett. **81**, 3599 (1998).
- [49] N. Fukunishi, T. Otsuka, I. Tanihata, Phys. Rev. C **48**, 1648 (1993).
- [50] I. Hamamoto, X. Z. Zhang, Phys. Rev. C **52**, R2326 (1995).
- [51] M. Yamagami, K. Matsuyanagi, M. Matsuo, Nucl. Phys. **A693**, 579 (2001).
- [52] J. Bardeen, L. N. Cooper, J. R. Schrieffer, Phys. Rev. **108**, 1175 (1957).



- P. G. de Gennes, *Superconductivity of Metals and Alloys* (Benjamin 1966).  
M. Tinkham, *Introduction to Superconductivity* (McGraw-Hill 1975).
- [53] A. Bohr, B. R. Mottelson, *Nuclear Structure* vol. II (Benjamin, 1975).
  - [54] F. Barranco, R. A. Broglia, H. Esbensen, E. Vigezzi, *Phys. Rev. C* **58**, 1257 (1998).
  - [55] S. T. Belyaev, A. V. Smirnov, S. V. Tolokonnikov, S. A. Fayans, *Sov. J. Nucl. Phys.* **45**, 783 (1987).

	$R_{surf}$ [fm]	$p(r_d)$		
		internal	surface	external
$^{22}\text{O}$	2.9	0.32	0.48	0.47
$^{58}\text{Ca}$	4.2	0.39	0.53	0.59
$^{84}\text{Ni}$	4.8	0.32	0.49	0.47
$^{44}\text{Ca}$	3.6	0.44	0.46	0.51
$^{66}\text{Ni}$	4.3	0.36	0.51	0.48

TABLE I: The di-neutron probability  $p(r_d)$  in  $^{22}\text{O}$ ,  $^{58}\text{Ca}$  and  $^{84}\text{Ni}$  near neutron drip-line, and in more stable  $^{44}\text{Ca}$  and  $^{66}\text{Ni}$ . The reference neutron position  $\mathbf{r}' = (0, 0, z')$  is fixed at the surface ( $z' = R_{surf}$ ), the internal ( $z' = R_{surf} - 2$  fm) and the external ( $z' = R_{surf} + 2$  fm) positions. The surface radius  $R_{surf}$  defined by the half central density of neutrons is also listed. The di-neutron probability is evaluated with  $r_d = 2$  fm except in the external case where we use  $r_d = 3$  fm. See also the text.

	$^{18}\text{O}$	$^{20}\text{O}$	$^{22}\text{O}$	$^{24}\text{O}$
$S^1/S_{TRK}^1$ ( $E < 15$ MeV)				
full pairing	6.8%	10.2%	13.6%	19.4%
no pairing	6.7%	9.3%	11.8%	19.8%
$B(\text{E1})$ [ $e^2\text{fm}^2$ ] ( $E_{th,1} < E < E_{th,1} + 4$ MeV)				
full pairing	0.188	0.254	0.393	0.702
no dynamical pairing	0.131	0.205	0.354	0.694
no pairing	0.104	0.175	0.235	0.718

TABLE II: The calculated energy weighted sum  $S^1 = \int_0^E dE' E' dB(\text{E1})/dE'$  of the E1 strength for the excitation energy below  $E = 15$  MeV in the oxygen isotopes, and  $B(\text{E1}) = \int_{E_1}^{E_2} dE' dB(\text{E1})/dE'$  [ $e^2\text{fm}^2$ ] in an excitation energy interval of 4MeV above the one-neutron threshold energy  $E_{th,1}$ . The value of  $S^1$  is given as a fraction to the Thomas-Reiche-Kuhn sum rule value  $S_{TRK}^1$ . We list also the results obtained without the neutron dynamical pairing correlation, and those neglecting all the neutron pairing correlations.

	$^{50}\text{Ca}$	$^{54}\text{Ca}$	$^{58}\text{Ca}$	$^{82}\text{Ni}$	$^{82}\text{Ni}$	$^{84}\text{Ni}$	$^{86}\text{Ni}$
$B(\text{E1})$ [ $e^2\text{fm}^2$ ]							
full pairing	0.73	1.48	1.76	1.39	2.17	3.01	3.72
no dynamical pairing	0.64	1.40	1.72	1.15	1.86	2.69	3.41
no pairing	0.68	1.86	1.83	1.27	2.25	3.21	5.11

TABLE III: The calculated E1 strength  $B(\text{E1}) = \int_{E_1}^{E_2} dE' dB(\text{E1})/dE'$  [ $e^2\text{fm}^2$ ] of the soft dipole excitation in Ca and Ni isotopes. In Ca isotopes the energy interval  $[E_1, E_2]$  is chosen with  $E_1 = 5.9, 5.2, 4.8$  MeV and  $E_2 = E_1 + 4$  MeV to enclose the soft dipole peak in  $A = 50, 54, 58$ , respectively. In Ni isotopes the interval with  $E_1 = E_{th,1}$  and  $E_2 = E_{th,1} + 5$  MeV is used. See also the caption of Table.II.

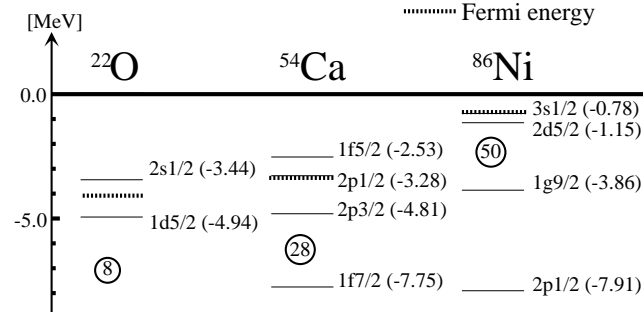


FIG. 1: The Woods-Saxon single-particle levels of neutrons in  $^{22}\text{O}$ ,  $^{54}\text{Ca}$  and  $^{86}\text{Ni}$ . The single-particle energy is indicated in the parenthesis. The Fermi energy obtained by the HFB calculation is drawn with the thick dotted line.

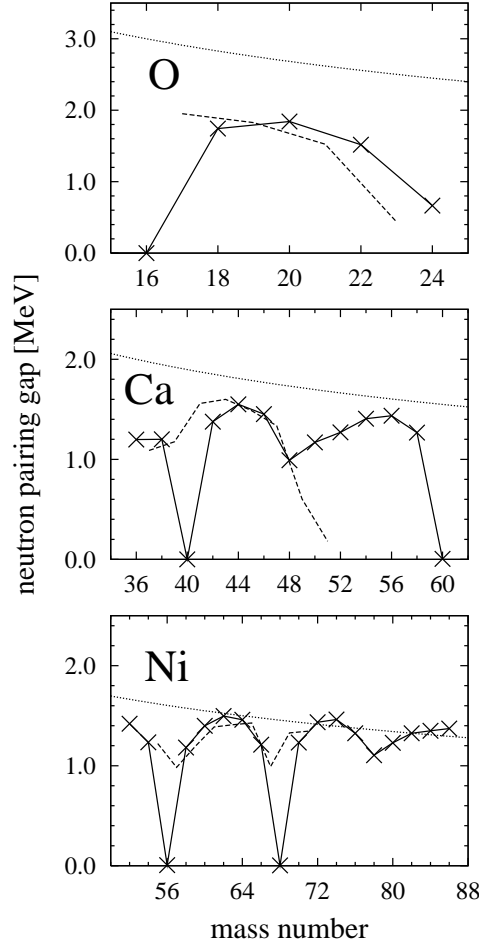


FIG. 2: The calculated neutron average pairing gap  $\langle \Delta_n \rangle$  in O, Ca and Ni isotopes, plotted with the crosses. The experimental odd-even mass difference evaluated with the three-point formula [48] is also shown by the dashed line. The dotted line is the conventional systematics  $\Delta_{sys} = 12/\sqrt{A}$  MeV of the pairing gap.

FIG. 3: The neutron two-body correlation density  $\rho_{corr,n}(\mathbf{r} \uparrow, \mathbf{r}' \downarrow) / \rho_n(\mathbf{r}' \downarrow)$  in  $^{22}\text{O}$ ,  $^{58}\text{Ca}$  and  $^{84}\text{Ni}$  calculated with the mixed pairing force is drawn on the  $x$ - $z$  plane. A contour plot of the same quantity is attached in the bottom of each panel where the interval of contour lines is  $0.001 \text{ fm}^{-3}$ . The symbol “X” on the  $x$ - $z$  plane indicates the position  $\mathbf{r}' = (0, 0, z')$  of the reference neutron. The results for  $^{22}\text{O}$ ,  $^{58}\text{Ca}$  and  $^{84}\text{Ni}$  are listed in the top, the middle and the bottom rows, respectively. In the middle column the reference neutron is fixed at the nuclear surface  $z' = R_{surf}$  whereas it is placed at the external position  $z' = R_{surf} + 2.0 \text{ fm}$  in the right column, and at the internal position  $z' = R_{surf} - 2.0 \text{ fm}$  in the left column. See Table I for the value of  $R_{surf}$ .

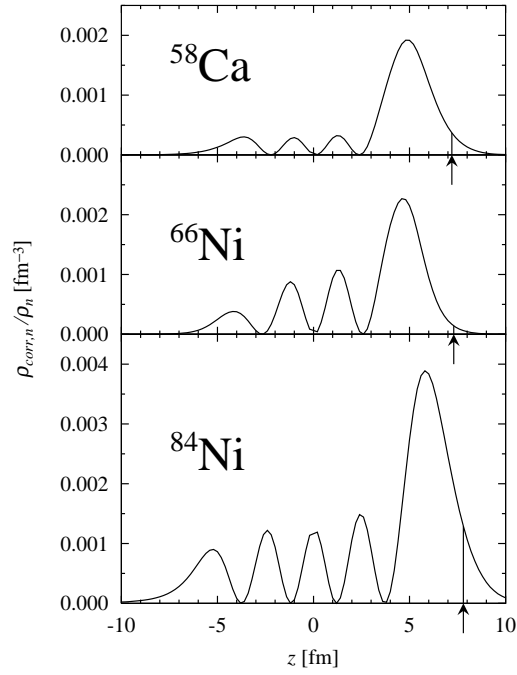


FIG. 4: The neutron two-body correlation density evaluated along the  $z$ -axis in near-drip-line nuclei  $^{58}\text{Ca}$  and  $^{84}\text{Ni}$ , and in a more stable isotope  $^{66}\text{Ni}$ . The reference neutron is fixed at  $z' = R_{surf} + 3 \text{ fm}$ , which is indicated by the arrows.

FIG. 5: The same as Fig.3 but for  $^{44}\text{Ca}$  and for  $^{66}\text{Ni}$ . The reference neutron is fixed at the surface position  $z' = R_{surf}$ .

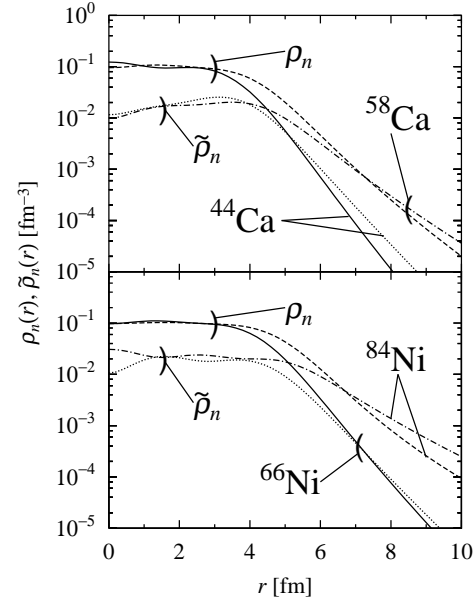


FIG. 6: The density  $\rho_n(r)$  and the pair density  $\tilde{\rho}_n(r)$  of neutrons in  $^{44,58}\text{Ca}$  and  $^{66,84}\text{Ni}$ . The solid and the dashed lines represent  $\rho_n(r)$  whereas the dotted and the dot-dashed lines are for  $\tilde{\rho}_n(r)$ .

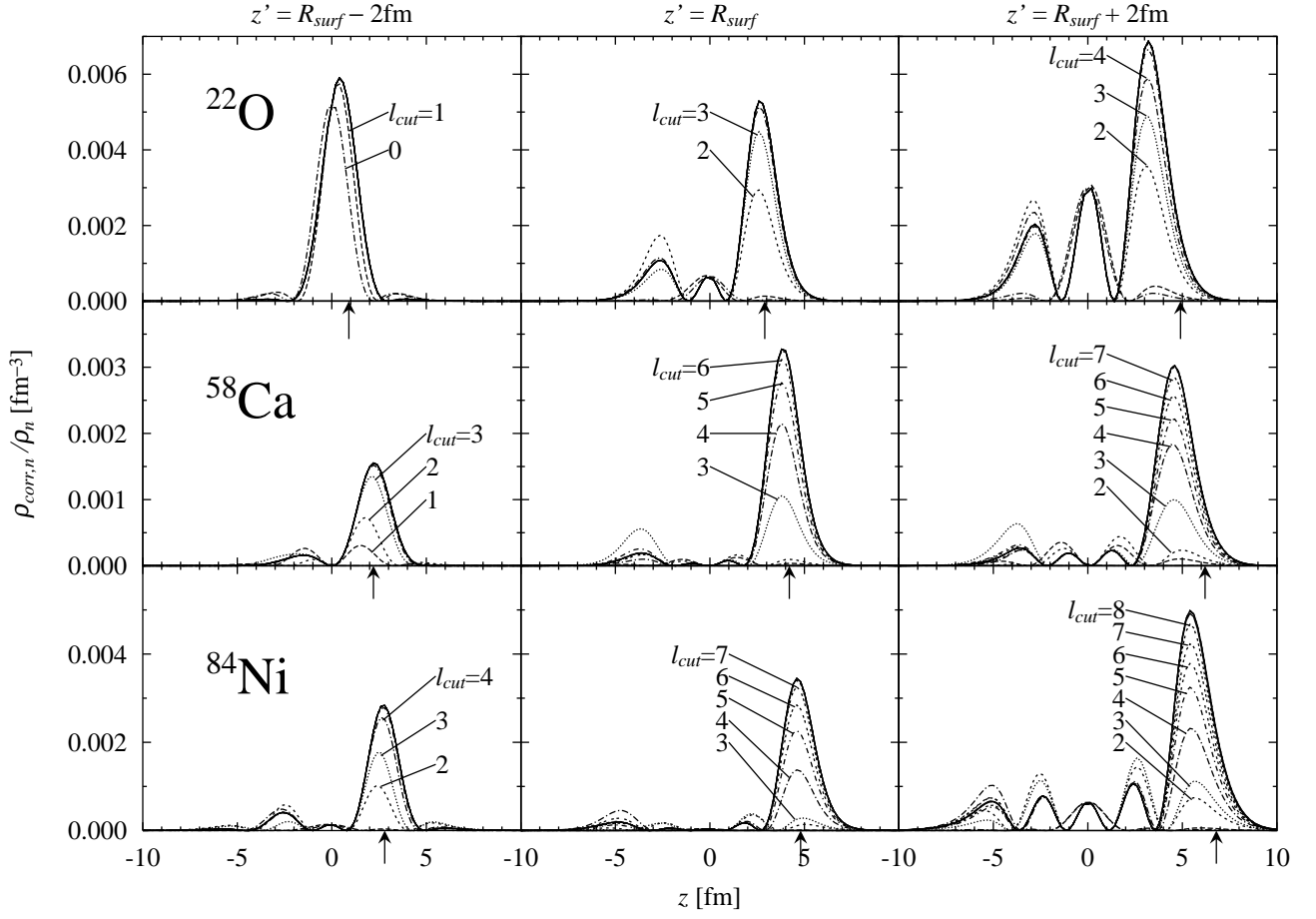


FIG. 7: The dependence of the neutron two-body correlation density on the orbital angular momentum cut-off  $l_{cut} = 0, 1, 2, 3, \dots$  for  $^{22}\text{O}$ ,  $^{58}\text{Ca}$  and  $^{84}\text{Ni}$  in the top, the middle and the bottom rows, respectively. The two-body correlation density is plotted along the  $z$ -axis. The full HFB result is drawn with the solid line. The reference neutron position is fixed at the internal ( $z' = R_{surf} - 2$  fm), the surface ( $z' = R_{surf}$ ) and the external ( $z' = R_{surf} + 2$  fm) positions in the left, the middle and the right columns, respectively. The arrows indicate the reference neutron position.

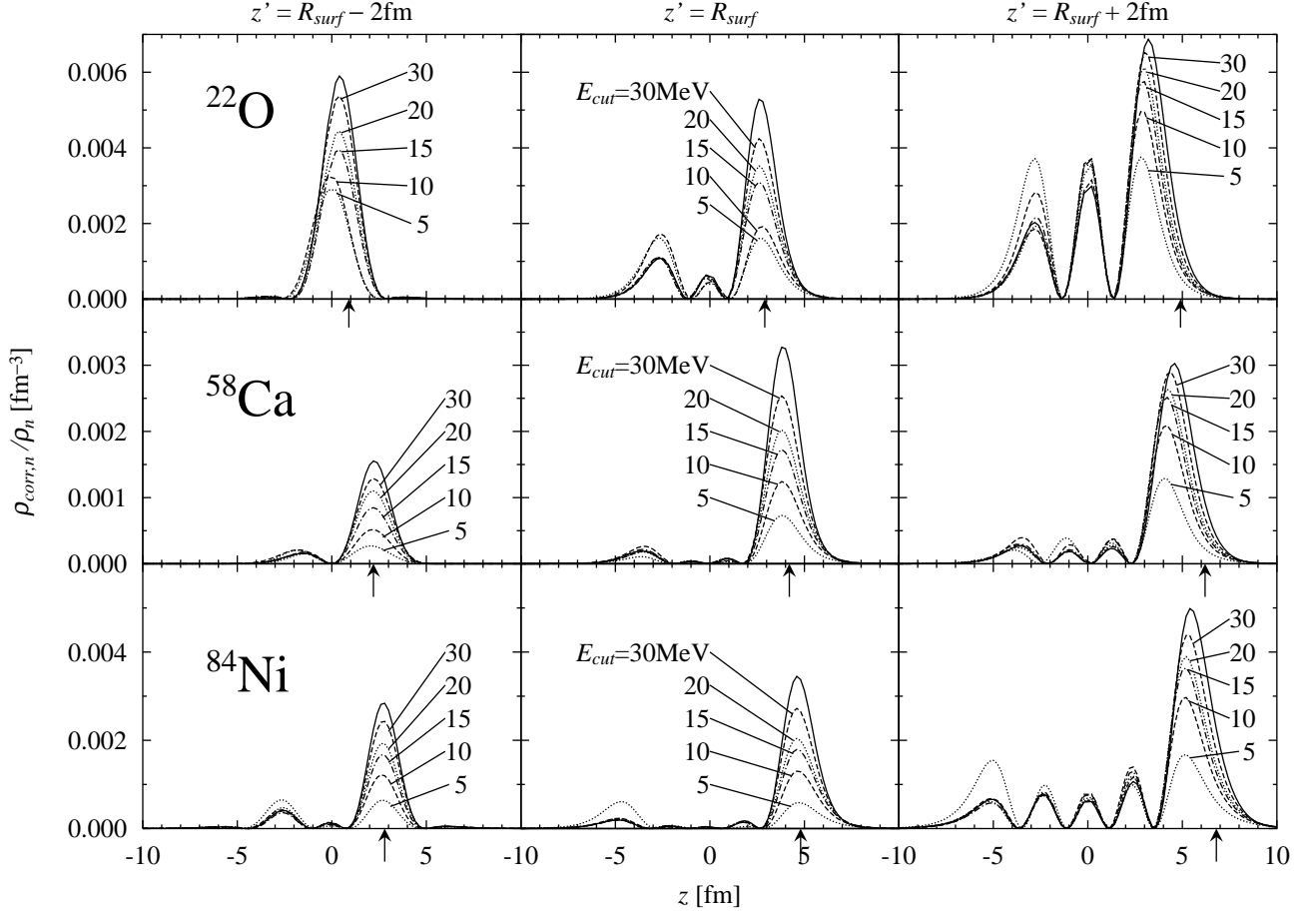


FIG. 8: The dependence of the neutron two-body correlation density along the  $z$ -axis on the quasiparticle energy cut-off  $E_{cut}$  for  $^{22}\text{O}$ ,  $^{58}\text{Ca}$  and  $^{84}\text{Ni}$ , to which the top, the middle and the bottom rows correspond respectively. The reference neutron fixed at the internal ( $z' = R_{surf} - 2$  fm), the surface ( $z' = R_{surf}$ ) and the external ( $z' = R_{surf} + 2$  fm) positions in the left, the middle and the right columns, respectively. The solid line represents the full HFB result.

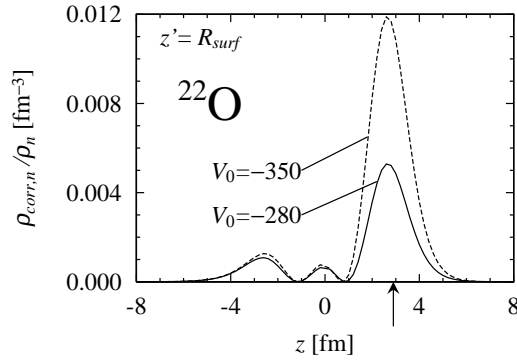


FIG. 9: The dependence of the neutron two-body correlation density on the pairing force strength  $V_0$  of the mixed pairing force in  $^{22}\text{O}$ . The solid line is the result with the reference value  $V_0 = -280$  MeV fm $^3$  corresponding to  $\langle \Delta_n \rangle = 1.5$  MeV whereas the dashed line is for  $V_0 = -350$  MeV fm $^3$  corresponding to  $\langle \Delta_n \rangle = 2.8$  MeV. The reference neutron is placed at the surface  $z' = R_{surf}$ .

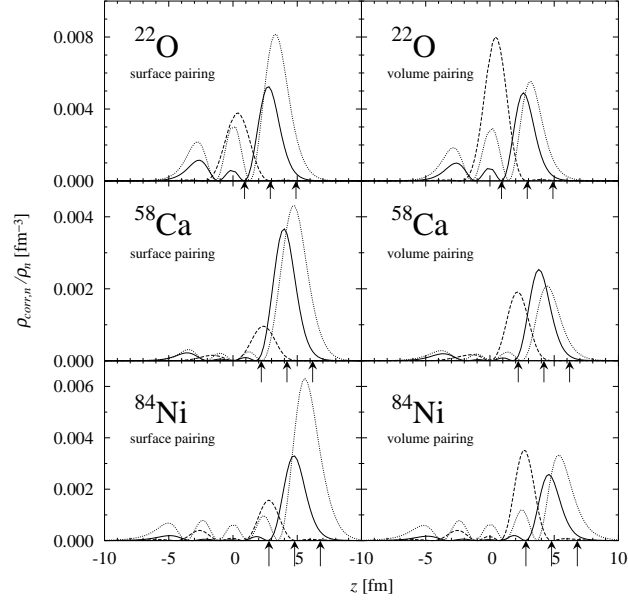


FIG. 10: The neutron two-body correlation density along the  $z$ -axis in  $^{22}\text{O}$ ,  $^{58}\text{Ca}$  and  $^{84}\text{Ni}$  calculated with use of the surface and the volume pairing forces having different density dependence. Here the dashed, the solid, and the dotted lines in each panel display this quantity for the internal, the surface, and the external positions of reference neutron. The pairing force parameters are:  $V_0 = -375, -395, -385 \text{ MeVfm}^3$  (in  $^{22}\text{O}$ ,  $^{58}\text{Ca}$  and  $^{84}\text{Ni}$ , respectively) and  $\rho_0 = 0.19 \text{ fm}^{-3}$  for the surface pairing, and  $V_0 = -190, -178, -180 \text{ MeVfm}^3$  ( $^{22}\text{O}$ ,  $^{58}\text{Ca}$ ,  $^{84}\text{Ni}$ ) for the volume pairing.

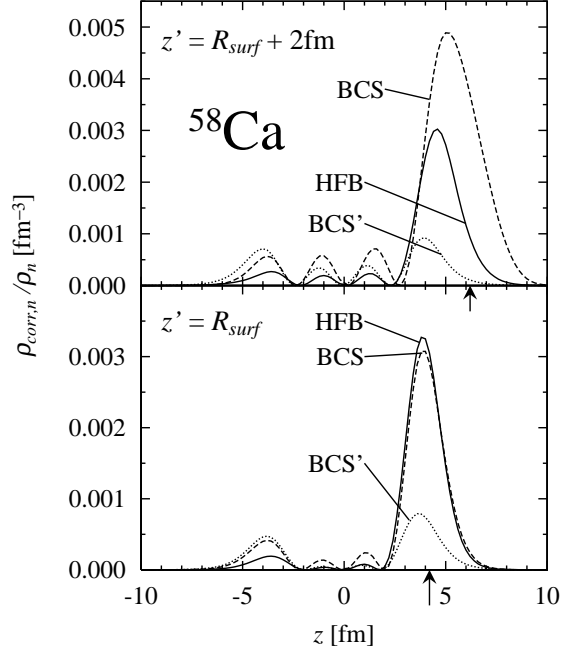


FIG. 11: The neutron two-body correlation density along the  $z$ -axis in the BCS approximation for  $^{58}\text{Ca}$  with use of a constant pairing gap  $\Delta_n = 1.27 \text{ MeV}$ , plotted with the dashed line. The HFB result (the solid line) is also shown for comparison. Another BCS result using only the bound Woods-Saxon neutron orbits is also shown by the dotted line (labeled with BCS'). The reference neutron is placed at the external position  $z' = R_{surf} + 2 \text{ fm}$  in the upper panel whereas it is at the surface  $z' = R_{surf}$  in the lower panel.



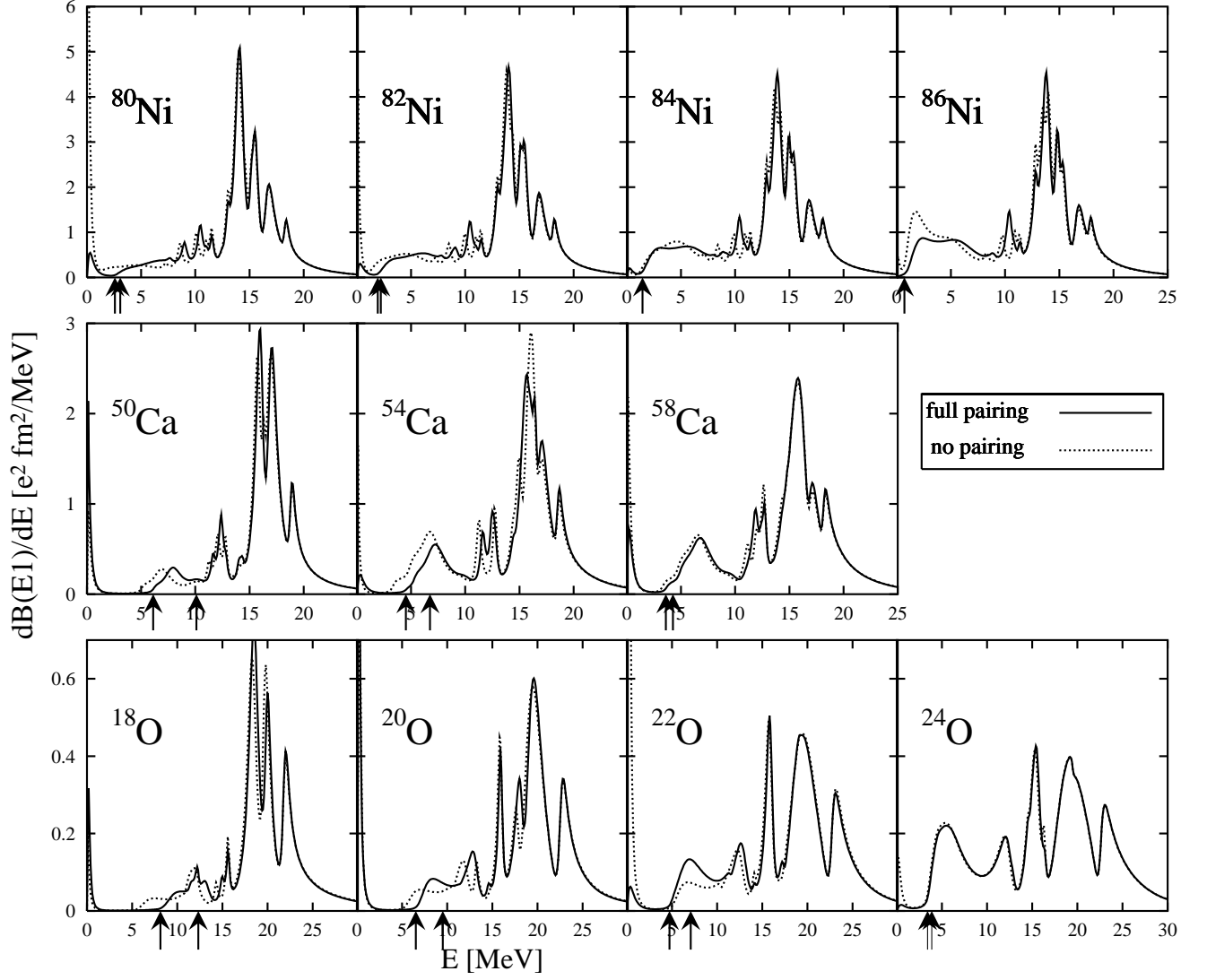


FIG. 12: The E1 strength function in the neutron-rich even-even oxygen, calcium and nickel isotopes near drip-line, calculated with use of the mixed pairing force and plotted with the solid line. The result obtained without the pairing correlation (by use of a very weak pairing force  $V_0 \approx 0$ ) is also plotted with the dotted line. The arrows indicate the one- and the two-neutron threshold energies  $E_{th,1}$  and  $E_{th,2}$ . Note that  $E_{th,1} = E_{th,2}$  in  $^{86}\text{Ni}$  and  $^{84}\text{Ni}$ , where there are no bound quasiparticle states for neutrons.

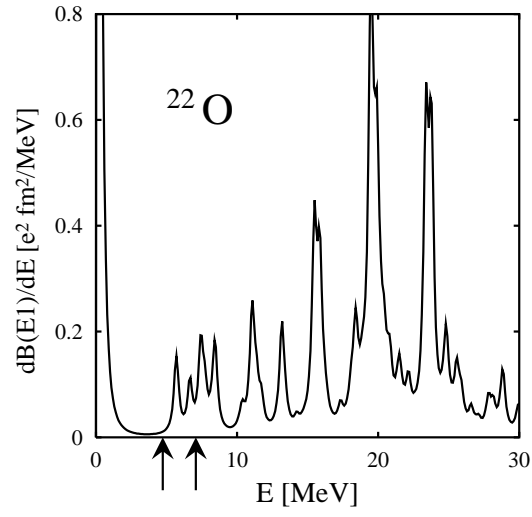


FIG. 13: The E1 strength function in  $^{22}\text{O}$ , obtained by using the discretized continuum states and the box boundary condition, in the case of the mixed pairing force. See also the text.

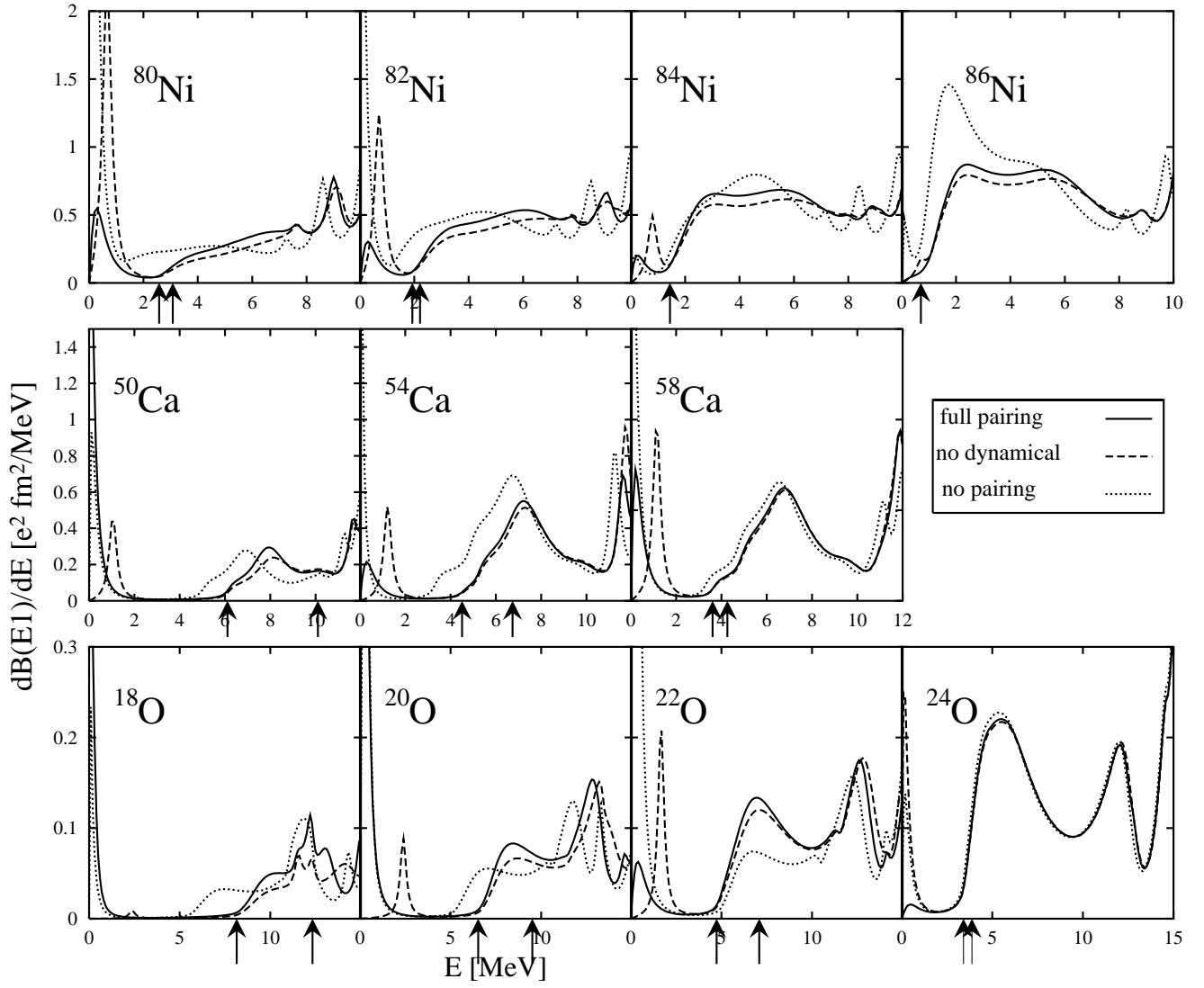


FIG. 14: The same as Fig.12, but emphasizing the low excitation energy region and effects of the static and the dynamical pairing correlations. For the latter purpose, the result obtained by neglecting the dynamical pairing correlation (while keeping the static pairing correlation) is plotted with the dashed line.

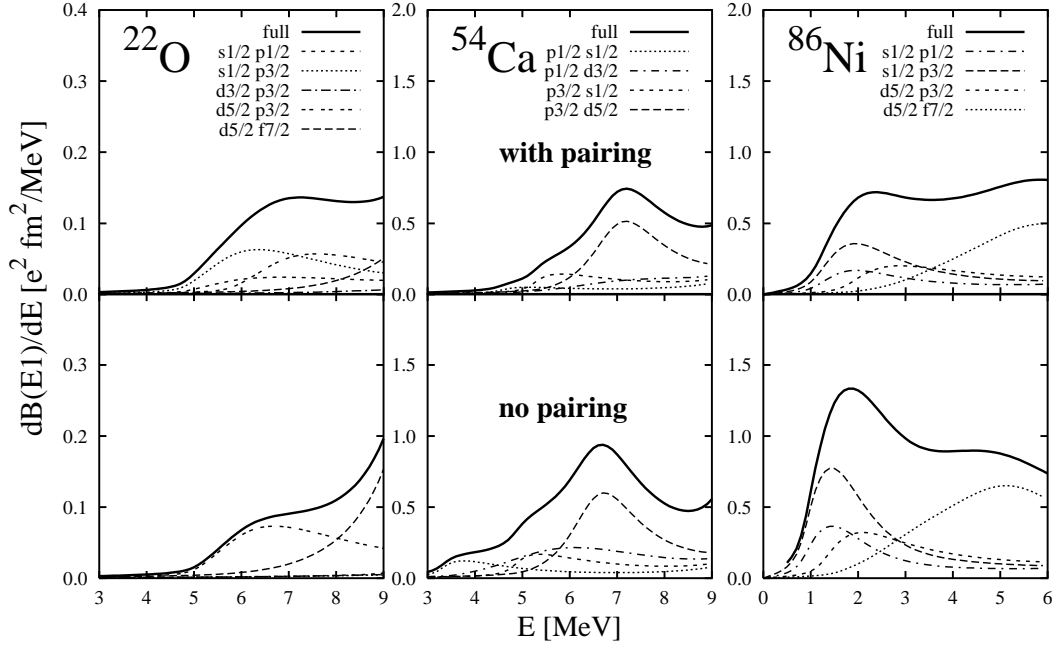


FIG. 15: The unperturbed E1 strength functions in  $^{22}\text{O}$ ,  $^{54}\text{Ca}$  and  $^{86}\text{Ni}$ . The upper panels display the unperturbed strength functions obtained with the mixed pairing force whereas in the lower panels the results without the pairing correlation is shown. The partial strengths selected by a pair of the angular momentum quantum numbers of the two-quasiparticle excitations are also plotted.

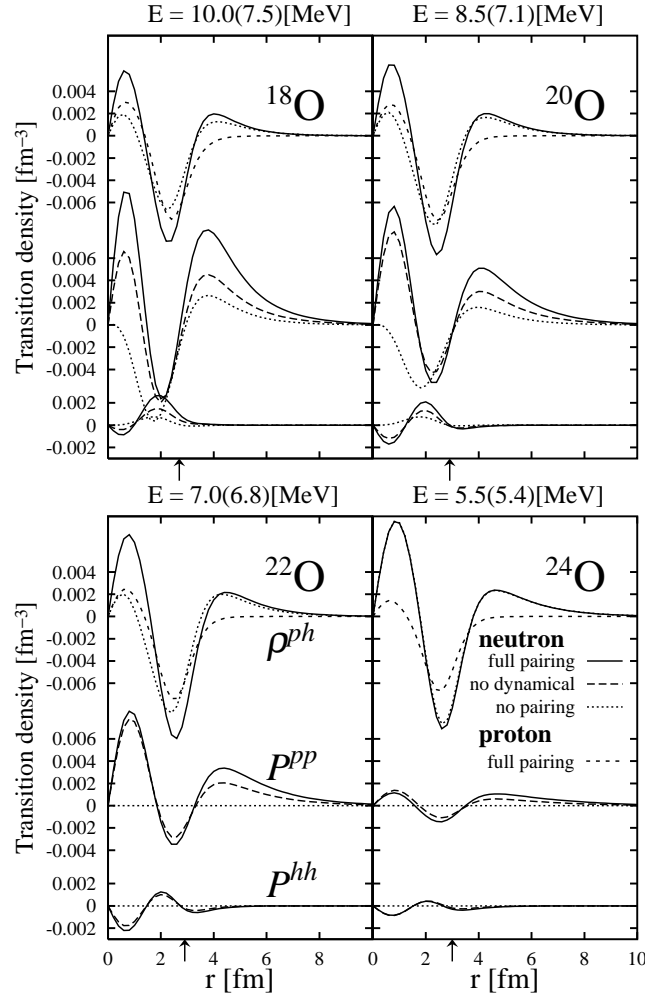


FIG. 16: The particle-hole transition density  $\rho_{iqL}^{ph}(r)$  (the top plot in each panel), the particle-pair transition density  $P_{iqL}^{pp}(r)$  (the middle plot) and the hole-pair transition density  $P_{iqL}^{hh}(r)$  (the bottom plot) of neutrons for the soft dipole excitation in the oxygen isotopes, plotted with the solid lines. The particle-hole transition density  $\rho_{iqL}^{ph}(r)$  of protons is also shown by the dashed line with wide intervals. For the pair transition densities  $P_{iqL}^{pp}(r)$  and  $P_{iqL}^{hh}(r)$ , the neutron amplitudes calculated by neglecting the dynamical pairing effect are also displayed with the dashed line. The dotted lines represent the neutron transition densities calculated by neglecting all the pairing correlations. The arrow indicates the surface radius (the half density neutron radius)  $R_{surf}$ . The selected excitation energy is  $E = 10.0, 8.5, 7.0, 5.5$  MeV for  $^{18,20,22,24}\text{O}$  ( $E = 7.5, 7.1, 6.8, 5.4$  MeV in the case of the no pairing calculation), which are indicated also in the figure. The  $B(E1)$  value listed in Table II is used for the normalization.

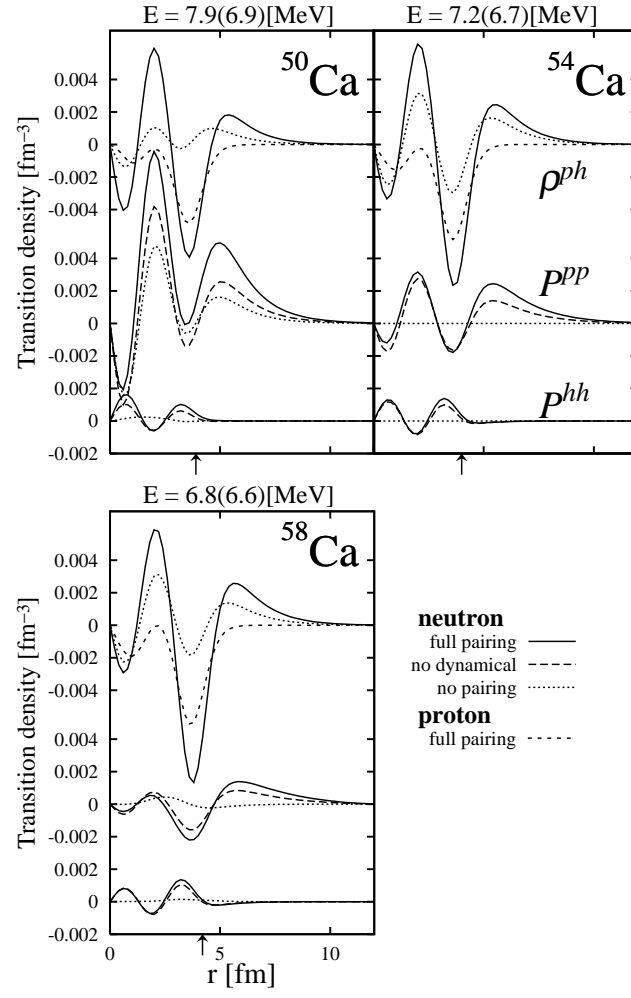


FIG. 17: The same as Fig.16, but for the calcium isotopes. The transition densities are evaluated at the peak energy of the soft dipole excitation indicated in each panel. The E1 strength listed in Table III is used for the normalization.

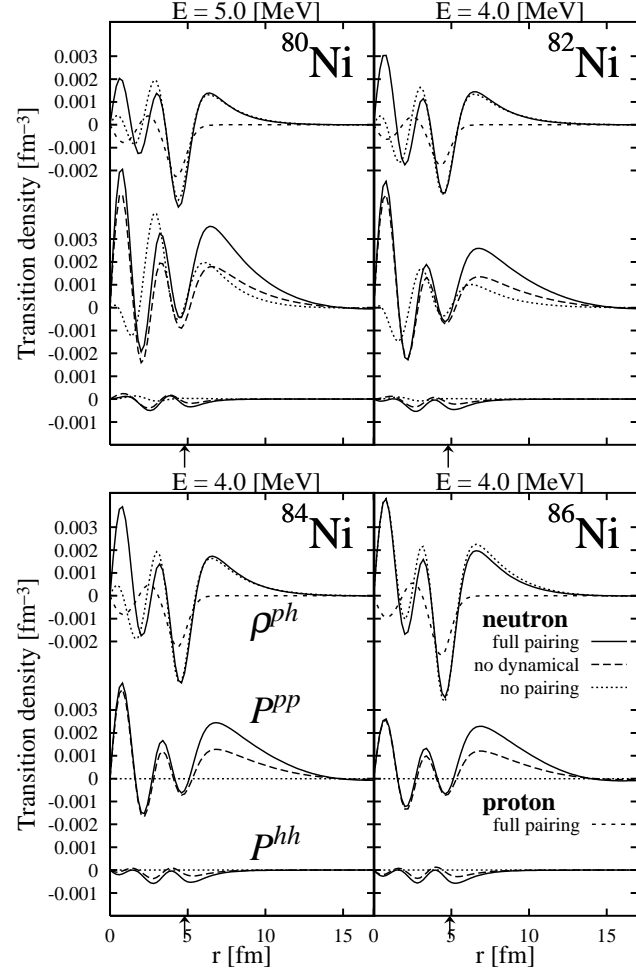


FIG. 18: The same as Figs.16 and 17, but for the nickel isotopes. The same excitation energy is used to calculate the transition densities with and without the pairing correlation.

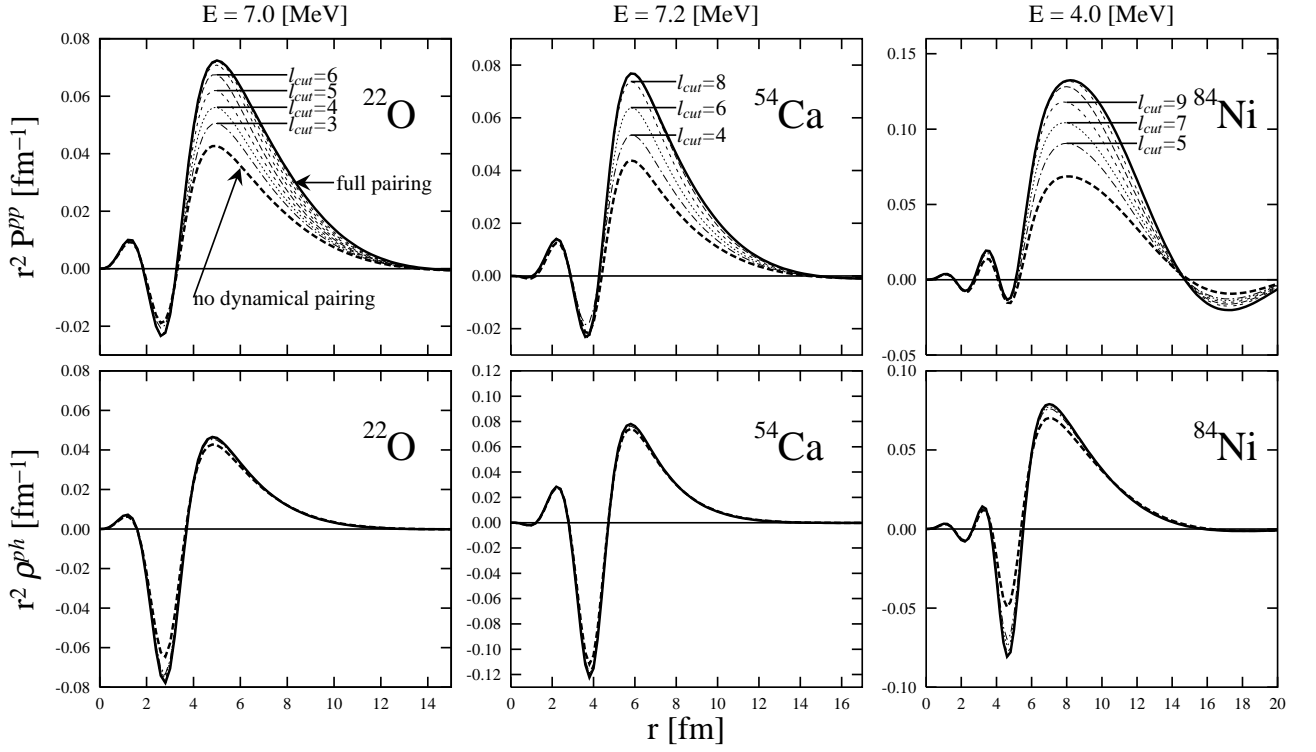


FIG. 19: The dependence of the particle-pair transition density  $r^2 P^{pp}(r)$  (in the top panels) and the particle-hole transition density  $r^2 \rho^{ph}(r)$  (in the bottom panels) of neutrons on the cut-off orbital angular momentum  $l_{cut}$  of the neutron quasiparticle states in  $^{22}\text{O}$ ,  $^{54}\text{Ca}$  and  $^{84}\text{Ni}$ . The results with  $l_{cut} = l_{cut}^0 (= 3), 4, 5, \dots, 9$  for  $^{22}\text{O}$ ,  $l_{cut} = l_{cut}^0 (= 4), 6, 8, 10$  for  $^{54}\text{Ca}$ , and  $l_{cut} = l_{cut}^0 (= 5), 7, 9, 11, 13$  for  $^{84}\text{Ni}$  are shown by thin lines. Here the volume element  $r^2$  is multiplied to magnify the amplitude in the external region. For reference sake, the result with the full pairing effects and the one without the dynamical pairing correlation are shown by the thick solid and the thick dashed lines, respectively.



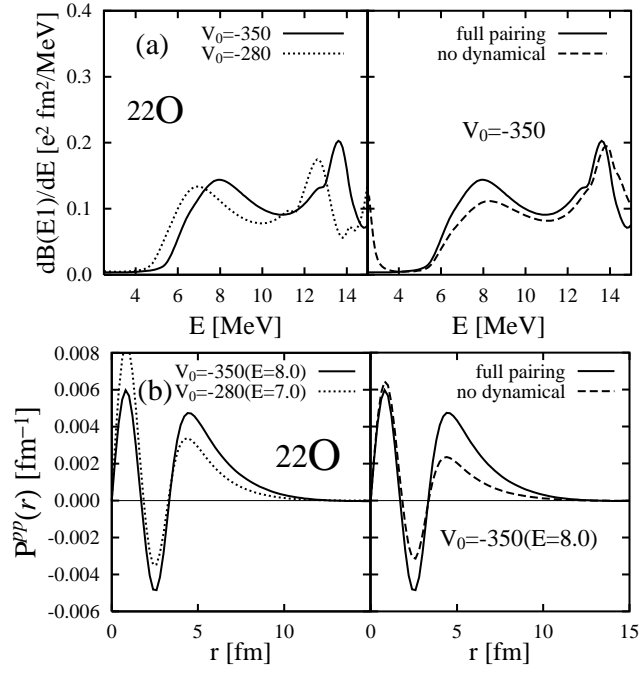


FIG. 20: (a) Dependence of the E1 strength function on the pairing force strength  $V_0$  of the mixed pairing force in  $^{22}\text{O}$ . The solid and the dotted lines are the results for  $V_0 = -350 \text{ MeV fm}^3$  and  $-280 \text{ MeV fm}^3$ , corresponding to the average neutron pairing gap  $\langle \Delta_n \rangle = 2.8 \text{ MeV}$  and  $1.5 \text{ MeV}$ , respectively. In the right panel, the result obtained by neglecting the dynamical pairing effect is plotted with the dashed line to visualize the dynamical pairing effect in the case of  $V_0 = -350 \text{ MeV fm}^3$ . (b) The same as (a), but for the particle-pair transition density  $P^{pp}(r)$  of neutrons.

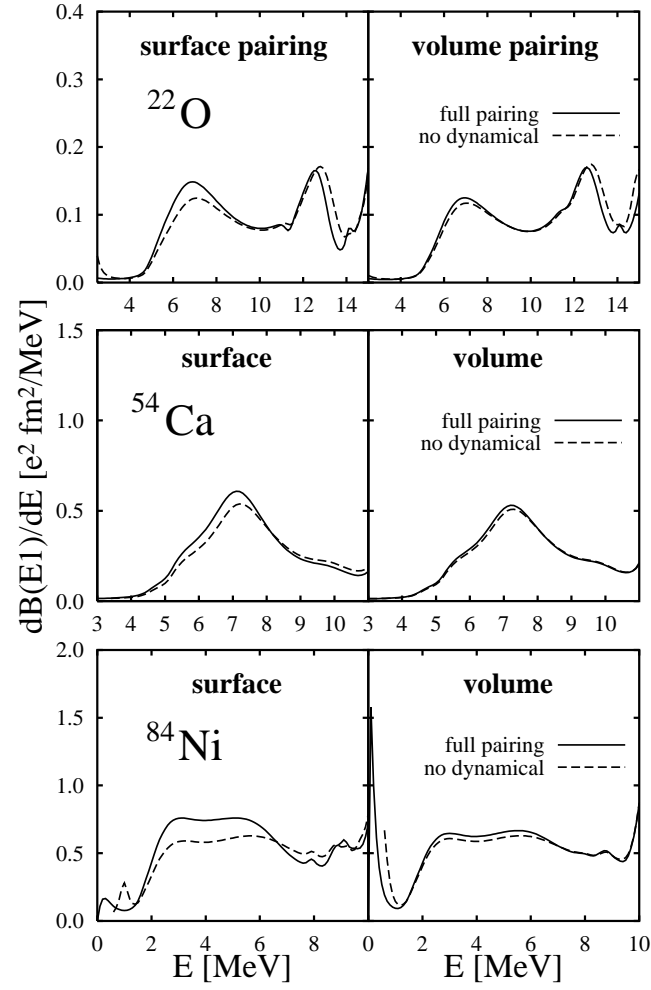


FIG. 21: The E1 strength functions in  $^{22}\text{O}$ ,  $^{54}\text{Ca}$  and  $^{84}\text{Ni}$  calculated with use of the surface and the volume pairing forces having different density dependence (the solid line). The left panels show results with the surface pairing with  $\rho_0 = 0.19 \text{ fm}^{-3}$  while the right panels are those with the volume pairing. The results with the full pairing effects is plotted with the solid line whereas the dashed line represents those without the dynamical pairing effect. See the caption of Fig.10 for the adopted force parameters.

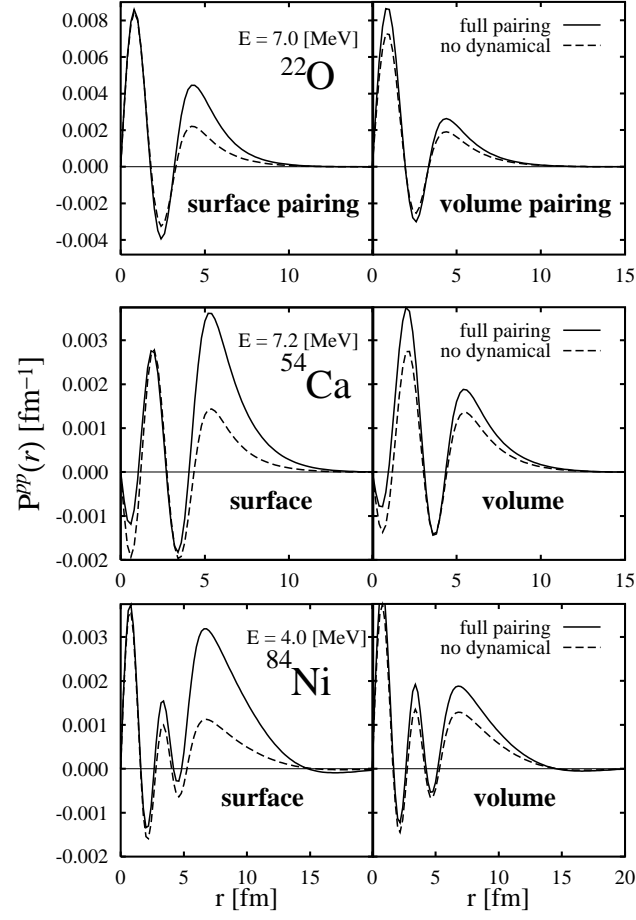


FIG. 22: The same as Fig.21, but for the particle-pair transition density  $P^{pp}(r)$  of neutrons associated with the soft dipole excitation at the excitation energy indicated in the figure.

This figure "fig3.jpg" is available in "jpg" format from:

<http://arxiv.org/ps/nucl-th/0408052v1>

This figure "fig5.jpg" is available in "jpg" format from:

<http://arxiv.org/ps/nucl-th/0408052v1>